Thin–Walled Structures 227 (2026) 115008

Contents lists available at ScienceDirect

Thin-Walled Structures

journal homepage: www.elsevier.com/locate/tws

Full Length Article

Numerical and analytical modelling of a novel hybrid ductile connection between FRP composite elements

Francesco Ascione [a,*], Mario D'Aniello [b], Alessandro Leonardi [a]

[a] *Dept of Civil Engineering, University of Salerno, Italy*
[b] *Dept. of Structures for Engineering and Architecture, University of Naples "Federico II", Italy*

ARTICLE INFO

Keywords:
Ductile connection
Hybrid connection
Numerical model
Mechanical model

ABSTRACT

This paper presents the findings of numerical and analytical parametric studies conducted to investigate the mechanical behaviour of a novel hybrid ductile connection for FRP composite elements. The hybrid joints examined—recently patented—are designed to bond FRP components to steel elements. These steel components are assembled using ductile bolted joints that are intentionally designed to be weaker than the adhesive, thus promoting a controlled ductile failure mode. Among all the steel elements, there is a channel acting as a structural fuse in which deformation is concentrated, which can be easily disassembled and replaced when necessary. The numerical simulations provide valuable insights into the development of plastic deformation within the steel fuse. Building on these results, analytical models were formulated to derive simple equations for estimating the elastic and post-elastic stiffness, as well as the ultimate strength of the hybrid joints, as a function of component geometry. Comparisons among analytical predictions, experimental tests, and numerical response curves show good agreement, confirming the practical applicability of the proposed approach.

1. Introduction

Bolted and bonded joints are commonly used to connect Fibre Reinforced Polymer (FRP) composite elements. Ideally, such connections should provide sufficient strength and ductility to fully exploit the mechanical properties of FRP profiles [1]. However, both technologies present limitations, including: (i) the need for holes that interrupt fibre continuity, (ii) the limited load-bearing capacity of pultruded profiles in bolted joints [2–13], (iii) the propensity for brittle failure, and (iv) the lack of reparability of bonded joints [14–18]. Hybrid connections have emerged as a promising solution to overcome these drawbacks. These systems typically pair over-designed FRP components—intended to remain undamaged—with weaker, ductile elements that are purposely designed to yield and provide the desired ductility. These weaker components, referred to here as "fuses," are often made of metals such as aluminium or steel and are assembled using bolted joints, while each metal component is adhesively bonded to its corresponding FRP part [19–23]. The term "hybrid" reflects both the combination of different materials (e.g., FRP and steel) and the integration of multiple joining technologies (e.g., adhesive bonding and bolting).

Some of the authors of this paper recently developed and patented a novel hybrid joint [24] in which FRP pultruded profiles are bonded to steel elements to preserve fibre continuity in the FRP elements. The steel components are bolted to additional steel parts that are intentionally designed to be weaker than the adhesive layer, thereby ensuring a ductile response. This configuration enables an optimised mechanical behaviour of all adopted materials, while remaining consistent with established construction practices for both FRP and steel structures.

Fig. 1 presents the geometry of this joint, which comprises: (1) a *nodal element* consisting of a steel section welded to an upper and lower end plate (shown as a red I-section, although a hollow section is also feasible); (2) a steel socket (blue) featuring an end plate, bolted to the nodal element and bonded to the FRP column; (3) a steel channel (green), intentionally designed as the weak component of the assembly; and (4) a steel T-joint (purple), bonded to the FRP beam (represented by the two yellow C-profiles) and bolted to the steel channel. This arrangement ensures (i) fibre continuity in the FRP elements bonded to the steel T-stub, (ii) ductility through yielding of the steel channel where plastic deformation is concentrated, and (iii) ease of repair due to the simple unbolting of components.

At least two bolt rows are used to connect the T-stub element to the steel channel (see Fig. 1). The number of rows and bolts is designed on

* Corresponding author.
E-mail address: fascione@unisa.it (F. Ascione).

https://doi.org/10.1016/j.tws.2026.115008
Received 24 September 2025; Received in revised form 26 February 2026; Accepted 20 April 2026
Available online 21 April 2026

the basis of the ultimate strength of the adhesive and the required performance of the joint.

The mechanical response of this type of joint has previously been investigated through an experimental campaign, whose main findings are reported in [24]. The satisfactory performance of the tested joints motivated the research presented in this paper. Indeed, to explore a wider range of parameters and monitor the local response of the joint components, a parametric finite element (FE) analysis was conducted using models validated against experimental results. In addition, analytical models were developed to predict the mechanical response of the joint, including its elastic and post-elastic stiffness and ultimate resistance.

For the sake of clarity, the article is organised into three main sections: (i) a concise overview of the experimental tests; (ii) a presentation and discussion of the numerical models and their results; and (iii) a description of the analytical models.

2. Concise overview of the reference experimental tests

This section concisely summarises the experimental program described in [24], providing the basic details about the properties of the materials, the test setup, the tested specimens, and the results obtained.

2.1. Materials

The GFRP beam and column are composed of a polyester matrix reinforced with glass fibres. The pultruded profiles were supplied by Top Glass Industries S.p.A. (Italy) [25], and their average mechanical properties are summarised in Table 1. All steel components were made from S275 JR grade steel, with an average yield stress of 312 MPa and an ultimate tensile stress of 456 MPa, as determined through coupon tests conducted on two specimens taken from the channel representing each thickness. Preloaded M12 grade 10.9 bolts were used, with an ultimate stress of 1195 MPa. Araldite AV 5308 (with Hardener HV 5309–1) [26] was employed as the adhesive material. This two-component epoxy adhesive is manufactured by Huntsman Advanced Materials (Switzerland) and supplied by Emanuele Mascherpa S.p.A. (Italy). The key mechanical properties of this structural adhesive are summarised in Table 1.

GRFP elements are made of an orthotropic, transversely isotropic material, where the 1–2 plane represents the plane of isotropy and the pultrusion axis (fibre direction) is aligned with the 3-direction, as illustrated in Fig. 2.

2.2. Test setup

All specimens represented an external corner beam-to-column subassembly, with boundary and loading conditions set accordingly. A monotonically increasing displacement was applied to the free tip of the beam using a rigid steel arm, which was clamped to the upper part of the testing machine. The Schenck Hydropuls servo-hydraulic universal testing machine was used (Fig. 3).

As illustrated in Fig. 3, the GFRP column was inserted into a steel jacket, which was clamped to the lower part of the testing machine. The static tests were conducted under displacement control at a rate of 2 mm/s. To monitor both the vertical displacement of the beam tip and the local deformations of each joint component, linear variable displacement transducers (LVDTs) were employed (Fig. 2).

2.3. Tested specimens

The specimens were designed to investigate the following parameters:

– The bond width (Lα) between the GFRP built-up beam and the steel T-Stub, as shown in Fig. 4a. Two values were considered: 150 mm and 220 mm.
– The thickness of the web of the steel channel (tβ, which was varied as follows: 2 mm, 3 mm, 4 mm, 5 mm, and 8 mm (see Fig. 4b).
– The pitch of the bolts connecting the steel T-Stub to the steel channel (dγ). As illustrated in Fig. 4c, two values were tested: 60 mm and 80 mm.

Variation of the above parameters resulted in 24 different geometries of the proposed joints. As three nominally identical specimens were produced and tested for each varied geometry, a total of seventy-two experimental tests were carried out. Each specimen was identified as DC-Lα-tβ-dγ-#δ, where:

– DC is for Ductile Connection.
– Lα for bonding width (e.g., L150 for the case of bonding width equal to 150 mm).
– tβ for the thickness of the web of the steel channel (e.g., t5 corresponds to the case with a thickness equal to 5 mm).
– dγ for the vertical pitch between holes of the steel channel (e.g., d60 for the case with pitch equal to 60 mm).
– #δ for the number of repetitive tests performed per configuration (e.g., #2 is the second test of the series of three nominally identical specimens).

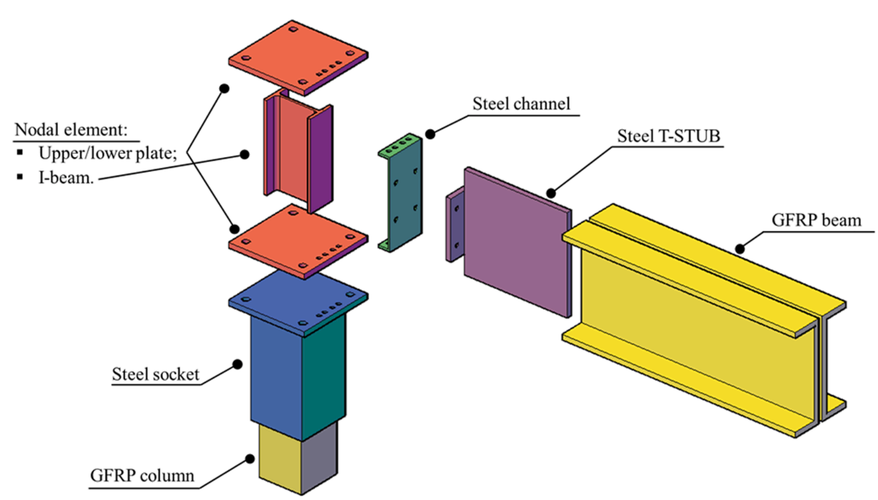

Fig. 1. The proposed hybrid connection and its main components.

Table 1
Mechanical properties of materials.

Material	Element Name	Young's Modulus [GPa]	Poisson's ratio [-]	Yielding Strength [MPa]	Shear Modulus [GPa]	Flexural Strength [MPa]	Tensile Strength [MPa]	Shear Strength [MPa]	G_{II}[27] [N/mm]
Steel	Nodal Zone Channel Socket	210.0	0.3	312.0	80.0	-	-	-	-
GFRP	Beam	27.5 (E_3)	0.09 ($\nu_{13}=\nu_{23}$)	-	3.0 ($G_{13}=G_{23}$) 3.86 (G_{12})	240.0	-	-	-
	Column	9.5 (E_1)	0.23 (ν_{12})						
Adhesive	-	-	-	-	-	-	30	10	4.10

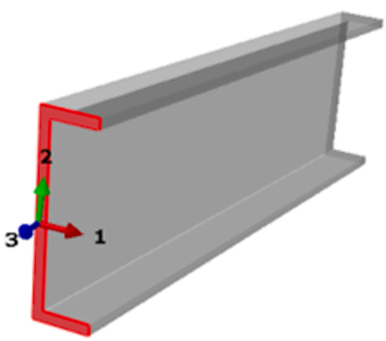

Fig. 2. GFRP system of reference: 1,2 is the plane of isotropy, axis 3 coincides with the fibre direction.

It is worth noting that the considered values of the bonding widths were chosen to be approximately two times (i.e., 150 mm) and three times (i.e., 220 mm) greater (for safety reasons) than the minimum required bond width (b_{eff}), which is approximately 70 mm according to Eq. (1):

$$b_{eff} = \frac{\pi}{2 \bullet \omega_s}; \omega_s^2 = \frac{\beta_{II}}{E_3 \bullet t_{adh}}; \beta_{II} = \tau_u / s_u. \tag{1}$$

In Eq. (1), τ_u and s_u are the shear limit strength and ultimate slip of the adhesive, respectively. Furthermore, E_3 is the elastic modulus along fibre direction, while t_{adh} is the thickness of the adhesive layer equal to 2 mm.

2.4. Experimental results

Experimental results are reported in Fig. 5 in terms of moment-rotation curves. It is possible to observe that both the resistance and stiffness of the joints are strongly influenced by the thickness of the steel fuse web. As expected, a thicker web leads to a stiffer and stronger joint, albeit with reduced ductility. This behaviour is directly linked to the

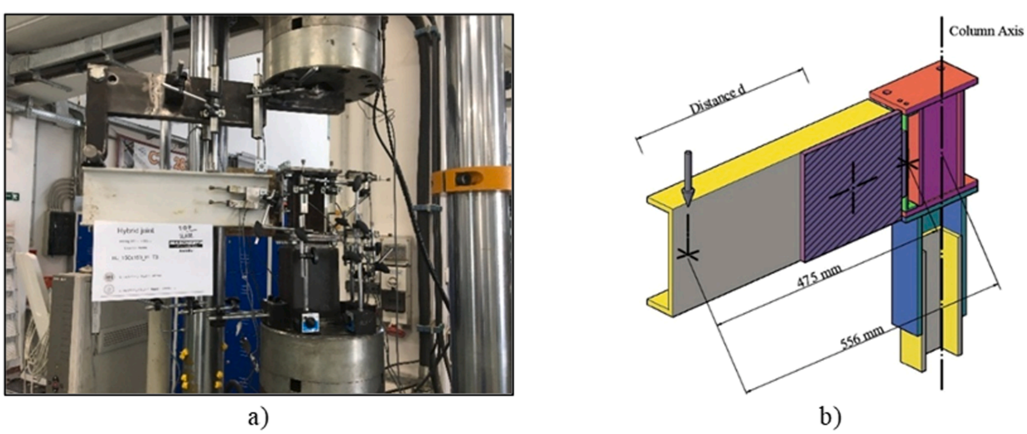

Fig. 3. The specimen ready to be tested: a) photo, b) schematic view.

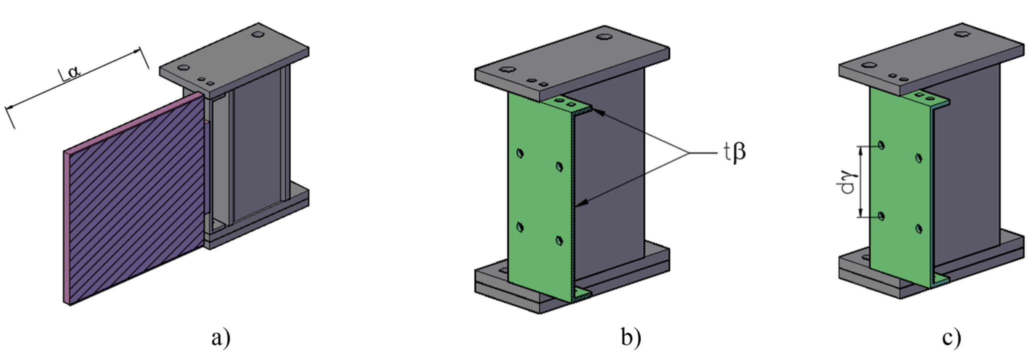

Fig. 4. Geometrical parameters of the specimens: a) bond length (Lα); b) thickness of the steel channel (tβ); c) pitch of bolts (dγ).

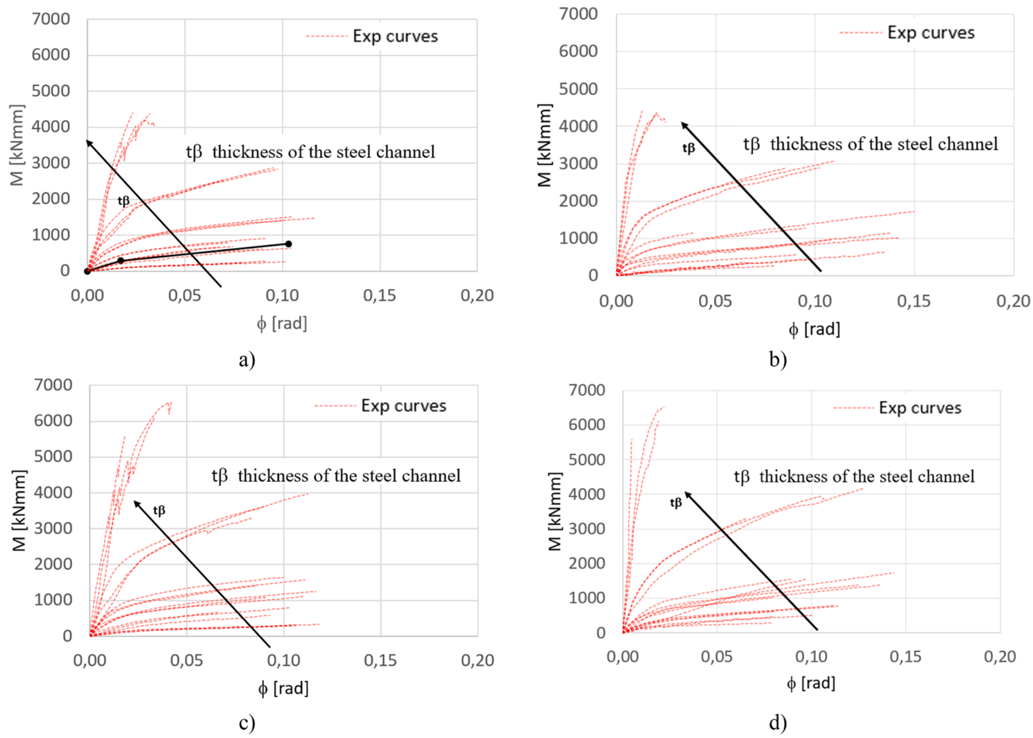

Fig. 5. Experimental results in terms of moment-rotation curves:a) DC-L150-d60; b) DC-L220-d60; c) DC-L150-d80; d) DC-L220-d80.

bending response of the steel fuse, whose strength and stiffness depend on the cross-sectional properties of the web plate.

Furthermore, Fig. 6 shows some photos of the tested specimens after the tests had finished. It is possible to observe the formation of plastic hinges in the steel channel only, while the adhesive layers remain intact, in line with the philosophy of the novel joint under investigation.

3. The FE models

3.1. Modelling assumptions

Finite element (FE) models were developed using Abaqus [28], with the geometrical details of the GFRP and steel components provided in Appendix A. The GFRP elements were modelled as orthotropic, transversely isotropic materials, as previously described in Section 2.1. The steel components were modelled using nominal values of Poisson's ratio and Young's modulus, together with the mean experimental true stress–true strain curves (see Fig. 7a). The von Mises yield criterion was adopted. The HR steel bolts were modelled following the approach described in D'D'D'Aniello et al. [29], assuming an ultimate tensile strength of 1195 MPa. In particular, both bolt head and nut were modelled using a linear elastic material constitutive law with E = 210 GPa and Poisson coefficient $\nu = 0.3$. The shank was modelled by meshing a solid cylinder having the nominal circular gross area of the bolt, where the plastic behaviour of the assembly is concentrated. The plasticity model was based on the multilinear true stress – true strain curve given in [29].

The interaction between the adhesive surfaces was modelled using cohesive laws ("surface-to-surface" interaction), as shown in Fig. 7b. In this model, τ_u denotes the ultimate shear stress, s_e is the relative sliding displacement between adherends at the elastic limit, and s_u is the sliding displacement corresponding to complete debonding.

$$G_{II} = \int_0^{s_u} \tau ds = \frac{1}{2}\tau_u \bullet s_u \tag{2}$$

The displacement is assumed to increase monotonically. Once damage initiates, the interface begins to soften and degrade. Interfacial damage starts when the quadratic nominal stress criterion is satisfied:

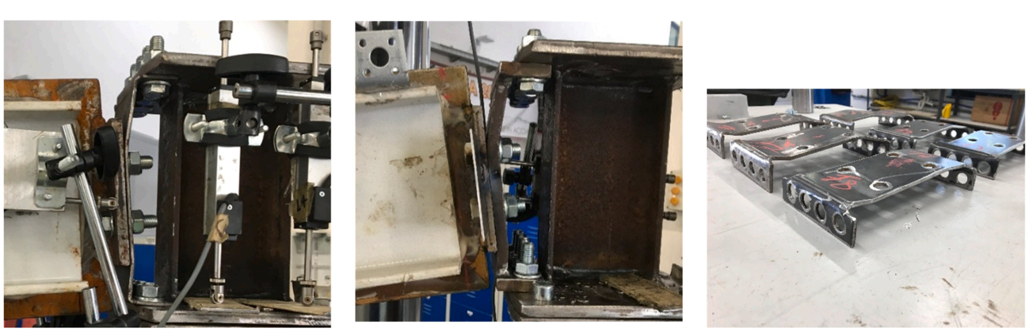

a) b) c)

Fig. 6. Photos of the collapse of the steel bolted channels (plastic hinges formation): a) thickness equal to 2 mm, b) thickness equal to 8 mm, c) steel channel deformation of repetitive tests.

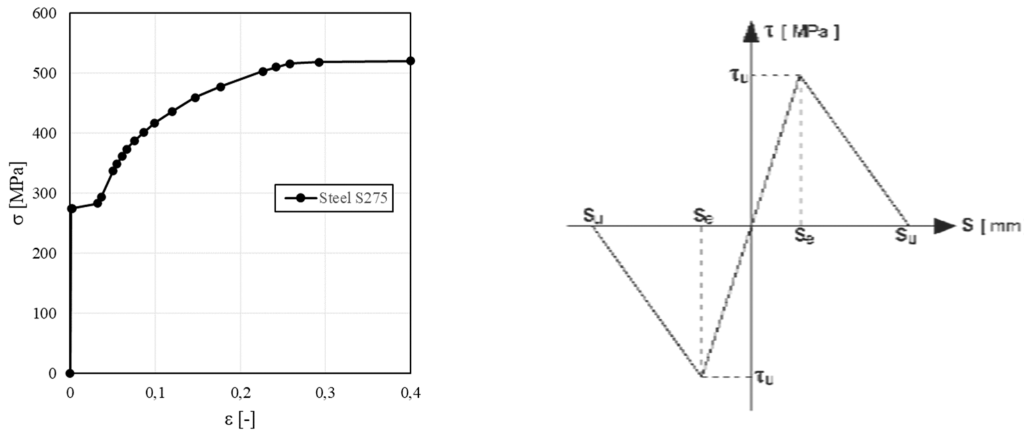

a) b)

Fig. 7. Model set-up: a) plastic behaviour of steel elements, b) traction separation law for the adhesive.

$$\left(\frac{\tau}{\tau_u}\right)^2 = 1 \tag{3}$$

The damage variable D assumes the following expression:

$$D = \frac{s_u \bullet (s - s_e)}{s \bullet (s_u - s_e)} \tag{4}$$

where s is the current sliding. From Eq. (4), it is easy to verify that if $s = s_e$, the damage variable is equal to zero; while, if $s = s_u$, the damage variable is equal to 1 (corresponding to complete separation between adherents, which are no longer connected by the adhesive layer).

The latter condition (D =1) corresponds to satisfying the following linear fracture criterion, here adopted:

$$\frac{G}{G_{II}} = 1 \tag{5}$$

The symbol G_{II} represents the work done by the traction (shear stress) and its conjugate relative displacement (sliding).

A linear eight-node hexahedral brick element with reduced integration (C3D8R) was used to model all components. To prevent interpenetration between components, all interfaces were modelled using the HARDCONTACT formulation. In addition, Coulomb friction was applied at the steel–steel interfaces, with a friction coefficient of 0.35, in accordance with Table 5.13 of the Eurocode 3 part 1–8 [30].

The welds between the I-beam and the upper and lower plates of the nodal element were modelled using a TIE interaction.

The boundary conditions are illustrated in Fig. 8. The fixity at the lower flange of the nodal zone was modelled by restraining all translational and rotational degrees of freedom at the centroid of the lower surface, using a rigid body constraint. Bolt clamping was modelled using the BOLTLOAD option, applying a tightening force of 47 kN, corresponding to the value specified by EN 1993–1−8 [30].

The load applied at the free end of the beam (Fig. 8) was introduced by prescribing a monotonically increasing vertical displacement. A dynamic implicit quasi-static analysis was performed, accounting for both geometrical and material nonlinearities.

To determine an appropriate finite element mesh, a preliminary sensitivity analysis was conducted by varying the mesh size from 9 mm (corresponding to approximately 20,000 elements) down to 2 mm (also approximately 190,000 elements), while monitoring the reaction force at the fixed constraint as shown in Fig. 8. For brevity, the sensitivity analysis was performed for the case where the steel channel web thickness t_β is 5 mm, the bolt spacing d_γ is 60 mm, and the bond length L_α is 220 mm. In In Fig. 9, the mesh sizes adopted are reported in round brackets.

The point marked with a triangle identifies the optimal mesh size (3 mm), corresponding to approximately 40,000 finite elements. This mesh size reflects the element-wise discretisation adopted in the study, as detailed in Tables 2 and 3.

Furthermore, in Table 3 are collected all mesh details for the steel channel only per each value of the thickness considered.

Fig. 10 shows the mesh for the bolts (a), the plates with holes (b), the

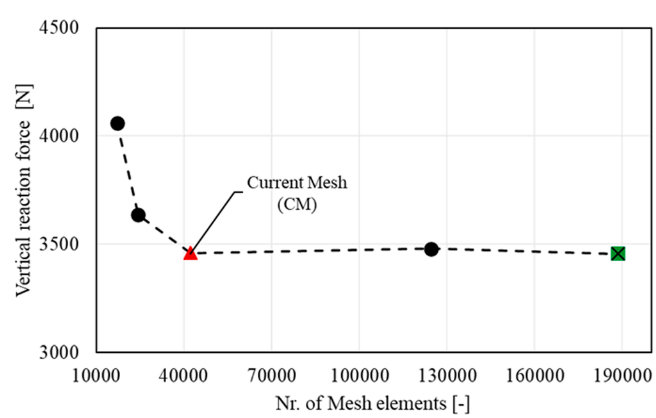

Fig. 9. Sensitivity analysis: number of mesh elements vs vertical reaction force.

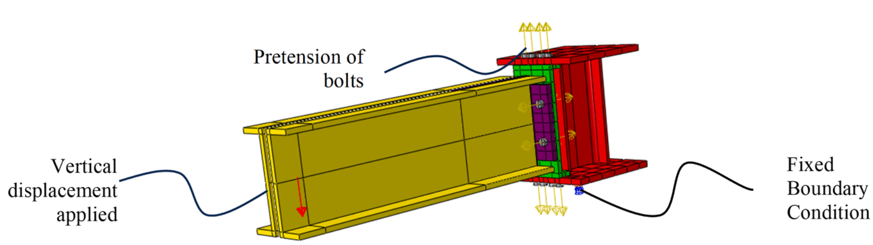

Fig. 8. Boundary and load conditions in the 3D numerical model.

Table 2
Number of finite elements along each direction for all components except for the channel element.

	head	shank	nut			
Single Bolt	3	8	3			
	web	flange	thickness	x-direction	y -direction	z-direction
T-Stub (plate with holes)	-	-	-	16	2	26
T-Stub (plate without holes)	-	-	-	2	48	30
Nodal Element (upper/ lower plate)	-	-	-	40	40	2
Nodal Element (I-profile)	14	14	2	-	-	36
GFRP C-profile	26	9	2	-	100	-

Table 3
Number of finite elements along each direction for the steel channel.

	web	flange	thickness	x direction	y direction	z direction
Thickness 2 mm	86	12	3	40	-	-
Thickness 3 mm	56	8	3	26	-	-
Thickness 4 mm	54	8	3	26		
Thickness 5 mm	84	14	3	41	-	-
Thickness 8 mm	40	7	3	22	-	-

entire connection (c), and the steel channel, GFRP C-profile, and steel I-profile (d). The GFRP column was not modelled, as it was fully inserted into the steel jacket during the experimental tests (see Fig. 3a).

The tightening of the bolts was simulated by means of the BOLT-LOAD option, which allows for imposing the preload into the mid inner section of the bolt shank. Fig. 11 shows the evolution of Von Mises stress pattern at the middle of the bolt shank from simple tightening, i.e., the condition (a) to the condition (c), which corresponds to the end of the overall flexural response of a joint.

In detail, in Fig. 11, three different stress patterns are depicted for three different load levels. Load level (a) refers to the elastic stage, (b) the post-elastic stage, while (c) refers to the ultimate value of the rotation imposed (0.13 rad).

3.2. Validation of the FE model

The comparison between the experimental and FE results in terms of moment–rotation curves is presented in Fig. 12. The moment M(vertical axis) is evaluated at the interface between the T-stub and the steel channel, and corresponds to the reaction force at the beam tip multiplied by a lever arm of 475 mm (see Fig. 3b). The rotation φ is calculated as the vertical displacement at the beam tip divided by the working length, which is also 475 mm (see Fig. 3b).

The main mechanical parameters of the experimental and numerical curves are evaluated on the basis of Fig. 13. In details, the elastic stiffness (K_{el}) is equal to the ratio (M_{el}/φ_{el}), where φ_{el} is the rotation corresponding to elastic resistance. The threshold of the elastic moment M_{el} is evaluated on the basis of the ECCS−45 procedure [31], namely as the intersection between the elastic stiffness and the tangent post-yielding stiffness, the latter having slope (K_p) equal to (K_{el}/10). All measured

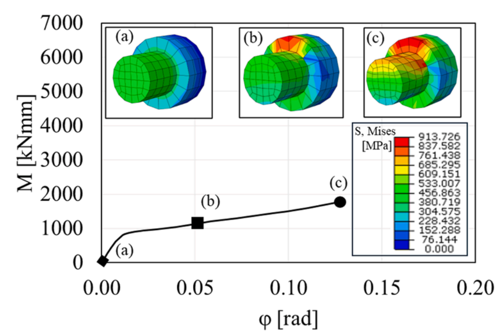

Fig. 11. Stress pattern along the bolt shank due to its pretensioning.

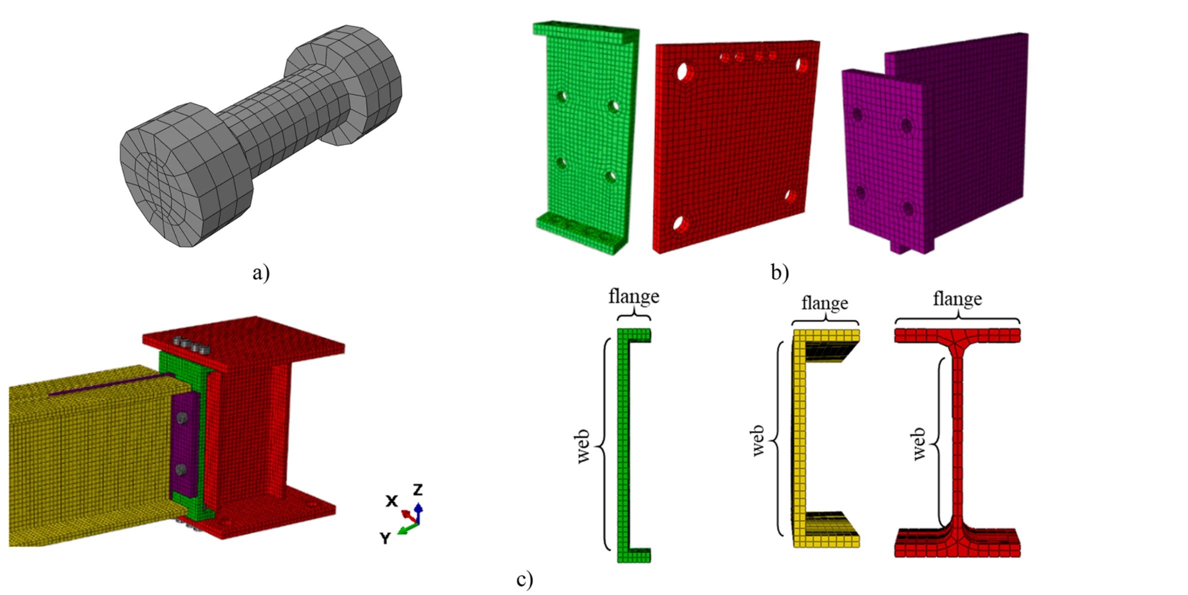

Fig. 10. Mesh of the dissipative connection: a) mesh of bolts; b) mesh of plates with holes; c) mesh of the assembled model and partition of C and I profiles.

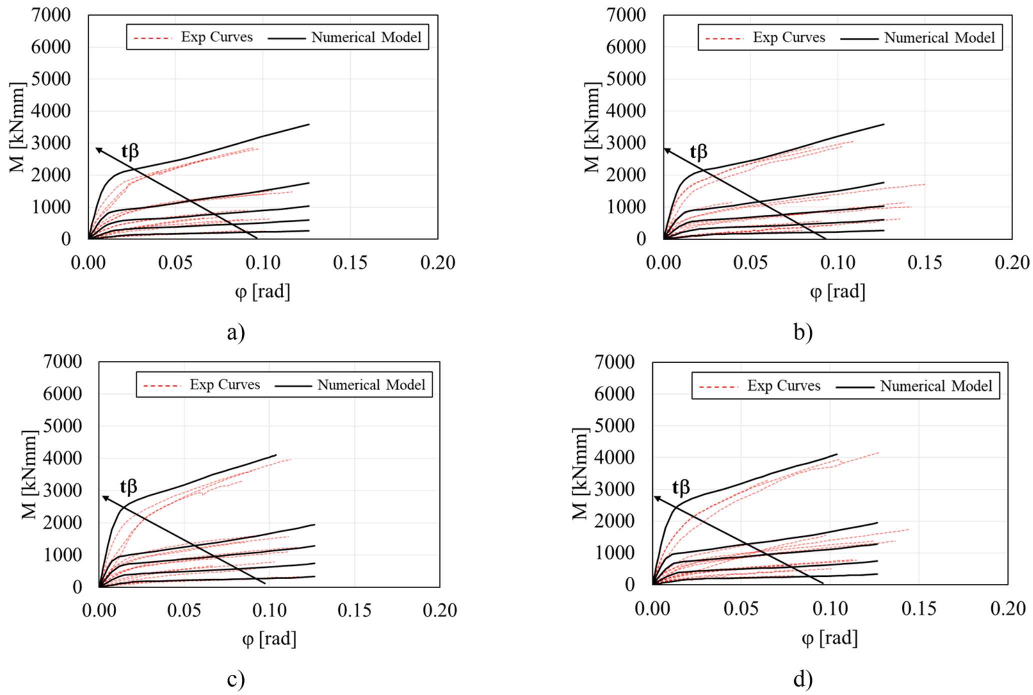

Fig. 12. Comparison between experimental and numerical results in terms of moments-rotations curves: a) DC-L150-d60; b) DC-L220-d60; c) DC-L150-d80; d) DC-L220-d80.

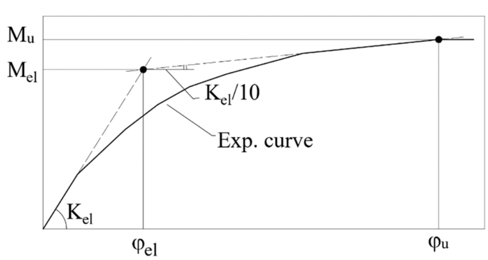

Fig. 13. Graphical procedure to evaluate the elastic resistance of the connection.

values are summarised in Table 4.

Furthermore, the comparison of the deformed configurations is presented in Figs. 14 and 15. Specifically, Figs. 14a and 15a show the deformed shape of the steel channel observed during the tests, while Figs. 14b and 15b illustrate the numerically predicted deformation of the steel channel for the specimens with web thicknesses of 2 mm and 8 mm, respectively. Finally, Figs. 14c and 15c depict the equivalent plastic strain (PEEQ in Abaqus), highlighting the locations of the plastic hinges.

Analysis of the deformed shapes across all modelled specimens shows that, irrespective of the bond length (L_α)and bolt pitch (d_γ), the number of plastic hinges depends primarily on the thickness of the steel channel web. For thin webs (2–5 mm), four plastic hinges were observed (Fig. 14c), whereas for the thicker web (8 mm), only three plastic hinges developed (Fig. 15c).

Overall, the FE models provide a satisfactory reproduction of the experimental behaviour. In line with the experimental observations, under all loading conditions, the steel components outside the fuse—namely the nodal element and the T-stub (Figs. 14b and 15b)—exhibit no significant deformation, with plasticity confined exclusively to the steel fuse.

3.3. *Parametric study: variation of the thickness of the steel channel*

To investigate the influence of the steel channel web thickness on the damage pattern and the evolution of plastic hinges, a parametric analysis was performed by increasing the web thickness as much as possible

Table 4
Comparison between Exp and Num results.

Series	t_β	Experimental results			Numerical results			Comparison Exp vs Num		
		M_{el} [kNmm]	φ_{el} [rad]	K_{el} [kNmm/rad]	M_{el} [kNmm]	φ_{el} [rad]	K_{el} [kNmm/rad]	ΔM_{el} [%]	$\Delta\varphi_{el}$ [%]	ΔK_{el} [%]
DC-L150-d60	4	475.000	0.009	5.168E + 04	522.500	0.012	4.513E + 04	16%	28%	14%
	5	670.700	0.009	7.409E + 04	855.000	0.012	7.384E + 04	10%	25%	17%
	8	1403.625	0.008	1.667E + 05	1710.000	0.009	1.846E + 05	8%	31%	33%
DC-L150-d80	4	712.500	0.014	5.174E + 04	655.500	0.011	5.999E + 04	8%	21%	14%
	5	916.275	0.014	6.696E + 04	817.000	0.009	9.240E + 04	11%	35%	28%
	8	2243.425	0.013	1.776E + 05	2232.500	0.010	2.256E + 05	0%	22%	21%
DC-L220-d60	4	475.000	0.009	5.168E + 04	475.000	0.009	5.168E + 04	13%	26%	15%
	5	670.700	0.009	7.409E + 04	670.700	0.009	7.409E + 04	14%	4%	10%
	8	1403.625	0.008	1.667E + 05	1403.625	0.008	1.667E + 05	18%	5%	14%
DC-L220-d80	4	763.800	0.014	5.582E + 04	665.000	0.012	5.707E + 04	13%	15%	2%
	5	815.813	0.012	7.046E + 04	831.250	0.008	1.012E + 05	2%	29%	30%
	8	2056.750	0.012	1.776E + 05	2137.500	0.009	2.256E + 05	4%	18%	21%

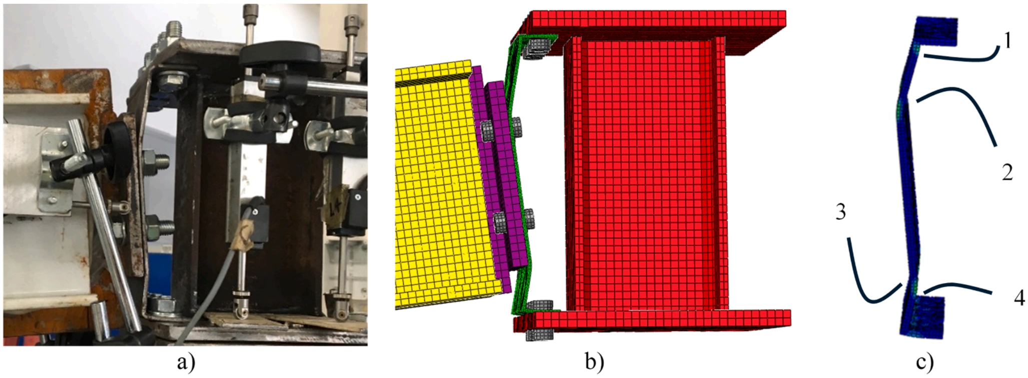

Fig. 14. Steel channel deformation (thickness equal to 2 mm): a) experimental test; b) deformed configuration; c) plastic hinges position.

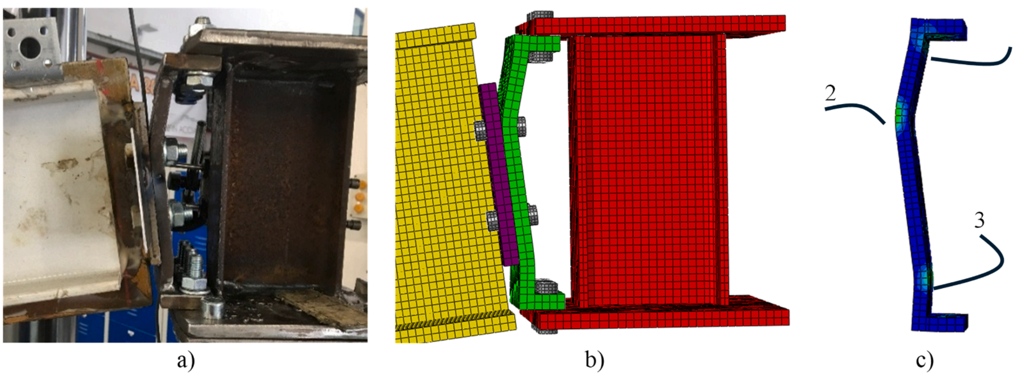

Fig. 15. Steel channel deformation (thickness equal to 8 mm): a) experimental test; b) deformed configuration; c) plastic hinges position.

without exceeding the design flexural capacity of the GFRP beam (see Appendix A). Since the steel channel must remain the weakest component of the joint, changes in its thickness required a redesign of all other steel elements, as detailed in Appendix B. A square hollow section (120 mm × 120 mm × 15 mm) was selected for the nodal element, replacing the I-section used in the experimental specimens (see Fig. 16). The thickness of the upper and lower plates was set to 20 mm, and their length was increased from 162 mm to 320 mm to satisfy EC3 requirements for minimum and maximum bolt spacing, as well as end and edge distances [29].

For the T-stub, the flange thickness (in contact with the channel web) and the stem thickness (bonded to the GFRP beam web) were set to 20 mm and 30 mm, respectively. The height of the T-stub was increased to match that of the fuse, improving the stiffness of the connection. Regarding the steel channel, four (two rows, Fig. 16a) or six (three rows, Fig. 16b) M16 bolts were used instead of the four M12 bolts adopted in the experimental program. Moreover, two rows of three M12 bolts replaced the original single row of four M8 bolts connecting the flanges to the upper and lower end plates of the nodal zone. Consequently, the depth of the fuse was increased from 80 mm to 140 mm. The GFRP geometries of the beam and column remained unchanged with respect to the experimental specimens.

The thickness of the T-stub element (t_T) was set equal to the thickness of the steel channel web (t_w). A ratio of three was adopted between the web thickness (t_w) and flange thickness (t_f) to promote the formation of plastic hinges in the flanges. The vertical bolt pitch in the steel channel was set to 60 mm, and the bond length to 220 mm.

Since the adhesive layer is stronger than the connected steel components (see Appendix B), it was modelled using a TIE interaction to reduce computational effort.

As described in Section 3.2, the load history was applied as a monotonically increasing displacement at the beam tip, with the maximum imposed displacement corresponding to a total chord rotation of 0.1 rad, consistent with the procedure adopted in the experimental tests.

In Fig. 17, the results of the numerical analyses for the full connection are presented as moment–rotation curves, as described in Section 3.2, for both configurations: two rows of two bolts (Fig. 17a) and three

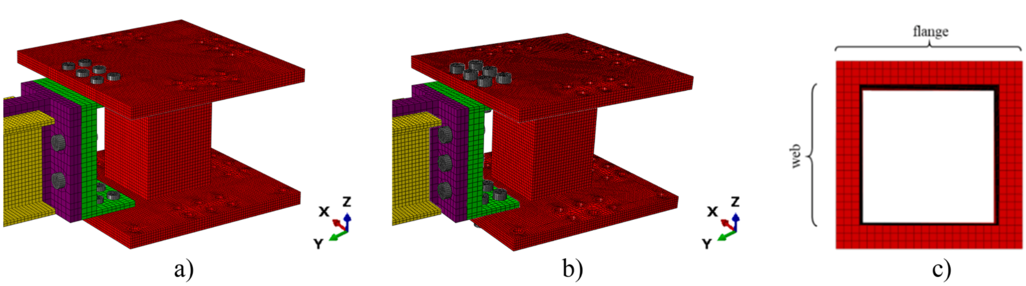

Fig. 16. Finite element model of the dissipative connection in the new configuration: a) 3D view (two rows of two bolts), b) 3D view (three rows of two bolts), c) new nodal element (hollow profile).

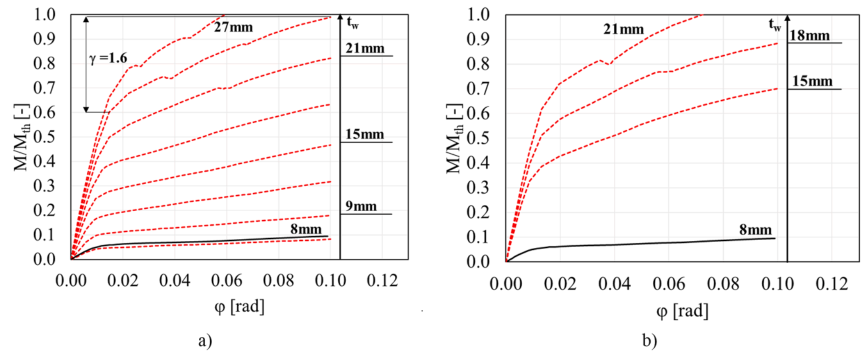

Fig. 17. Numerical moment-rotation curves varying the thickness of the web of the steel channel: a) two rows of two bolts; b) three rows of two bolts.

rows of two bolts (Fig. 17b). To highlight the role of the GFRP beam, the numerical moments have also been normalised by the beam's theoretical ultimate moment, calculated by the well-known Navier's formula, taking into account the geometry of Appendix A (Figure A1) and the GFRP flexural strength $\sigma_{f,l}$ (Table 1).

$$M_{th} = \frac{\sigma_{f,l} \bullet I_x}{(h/2)} = \frac{240 \quad MPa \bullet 10474859 \quad mm^4}{75 \quad mm} = 33.52 \quad kNm \tag{6}$$

It can be observed that increasing the web thickness of the steel channel results in higher stiffness and resistance for all connection configurations, although in some cases the overall response becomes limited by the capacity of the GFRP beam. For the configuration with two rows of two bolts (Fig. 16a), the connection with $t_w = 27$ mm reaches its ultimate rotation earlier than the other curves. In contrast, for the configuration with three rows of three bolts (Fig. 17b), this behaviour occurs for a web thickness of $t_w = 21$ mm. For all remaining cases, the ultimate moment corresponds to the previously defined ultimate rotation, as the resistance of the GFRP beam is sufficient to ensure that the steel channel remains the weakest component of the connection. Both figures also allow comparison between the new configurations and the experimental setup, which employed a web thickness of 8 mm.

Furthermore, the numerical results show that the number and location of plastic hinges remain unchanged regardless of the steel channel thickness or the number of bolt rows (see Figs. 18–20).

In details, Figs. 18–20 depict the equivalent plastic strain (PEEQ in Abaqus), highlighting the locations of the plastic hinges, for the case of two rows of two bolts and thickness of the web equal to 6 mm (Fig. 18), for the case of two rows of two bolts and thickness of the web equal to 27 mm (Fig. 19), for the case of three rows of two bolts and thickness of the web equal to 18 mm (Fig. 20).

Ultimately, three plastic hinges are consistently identified: plastic hinge #1 on the upper flange of the steel channel, plastic hinge #2 on the upper row of bolts (in tension according to the test setup in Fig. 2a), and plastic hinge #3 on the lower flange of the steel channel. Therefore, the plastic hinge mechanism of the proposed joint can be considered stable and consistent across all investigated geometries.

4. Analytical modelling of the bolted channel connection

4.1. Mechanical model to estimate the resistance

The ultimate resistance of the steel channel is estimated by applying the principle of virtual work to the equivalent structural layout shown in Fig. 21. The channel is idealised as an equivalent portal frame, where the web is modelled as the beam element, the flanges are modelled as the columns, plastic hinges are assumed to develop at the upper flange, lower flange and at the web level of the upper bolt row, consistently with the FE results (Figs. 18–20).

The plastic moments at the hinges located in the flanges and in the web are denoted as $M_{0,f}$ and $M_{0,w}$, respectively. It is important to clarify that in the redesigned configuration (Section 3.3), the flange thickness t_f was assumed equal to three times the web thickness t_w. This design choice was adopted to ensure that plastic deformation localises in the flanges while maintaining the intended global mechanism. Consequently, assuming a rectangular section and a fully plastic stress distribution, both $M_{0,f}$ and $M_{0,w}$ can be expressed as functions of t_w only as reported in Eq. (7).

$$M_{0,f} = \frac{f_y \, l \, t_w^2}{36}; M_{0,w} = \frac{f_y \, l \, t_w^2}{4} \tag{7}$$

where f_y is the steel yield strength, t_w is the thickness of the web of the steel channel, and l is the width of the steel channel.

Therefore, based on the plastic pattern shown in Fig. 17, the equilibrium can be solved through the following equation:

$$M\varphi_2 = (M_{0,f} + M_{0,w})(\varphi_1 + \varphi_2) \tag{8}$$

The meaning of the symbols is explained in Fig. 17. Through algebraic manipulations, the rotations φ_1 and φ_2 can be expressed as functions of the geometrical parameters as follows:

$$\varphi_1 = \frac{2\delta}{h - d\gamma}; \varphi_2 = \frac{2\delta}{h + d\gamma} \tag{9}$$

Substituting Eq. (9) into Eq. (8), the moment that triggers the intended plastic mechanism can be easily derived in closed form (Eq. 10).

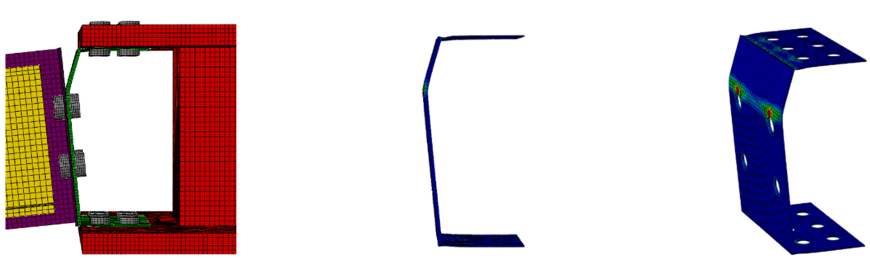

Fig. 18. Plastic hinges position for two rows of two bolts and the thickness of the web (6 mm).

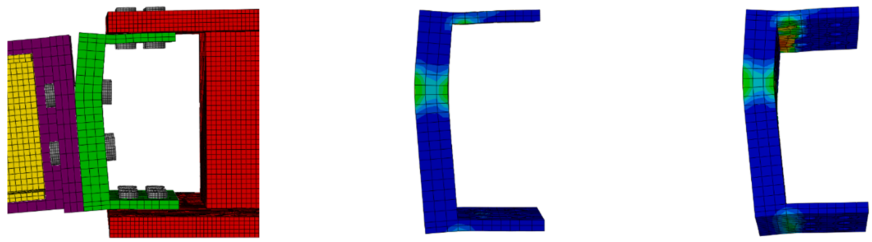

Fig. 19. Plastic hinges position for two rows of two bolts and the thickness of the web (24 mm).

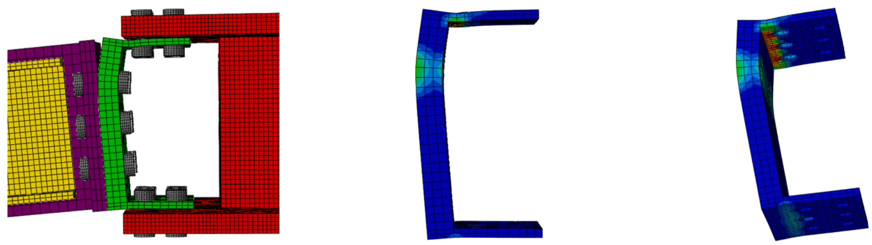

Fig. 20. Plastic hinges position for three rows of two bolts and the thickness of the web (21 mm).

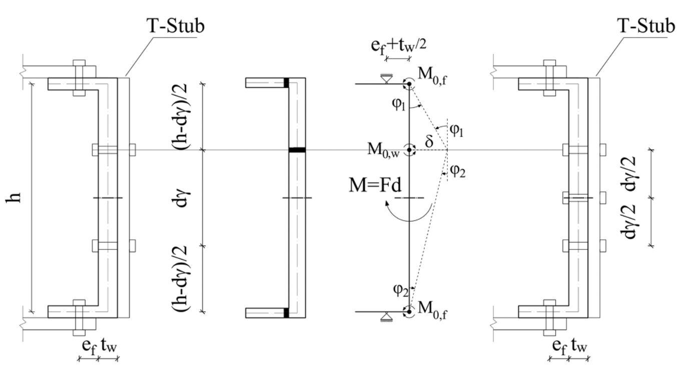

Fig. 21. Plastic kinematism of the steel bolted channel due to the expected locations of the plastic hinges.

$$M = f_y l t_w^2 \frac{5}{9} \frac{h}{h - d_\gamma} \tag{10}$$

The analytical estimation of the ultimate moment for all the investigated cases is given in Table 5.

4.2. Mechanical model to estimate the stiffness

The elastic stiffness of the bolted steel channel was estimated using the structural schemes shown in Fig. 22. For evaluating the elastic rotation (see Appendix C) at point B where the external moment M is applied, two alternative models are defined depending on the ratio between the tensile force per bolt (M/d_γ) and the bolt preload force, F_{Pl} (see Model 1 and 2 in Fig. 22). The reference static scheme is the equivalent portal frame introduced in the previous section.

The tensile force per bolt is calculated by dividing the applied moment M by the bolt pitch d_γ as shown in Fig. 22, while the bolt preloading force F_{Pl} was determined according to EN 1993–1–8 [30] (see Appendix B for the definition of relevant symbols of Eq. 11) and was set to 94 kN in the calculation shown in this study.

$$F_{Pl} = \frac{0.7 \quad f_{ub} A_s}{1.1} \tag{11}$$

In the case of Model 1 (see Fig. 22), the T-stub and channel web remain in contact along the entire height AC. This behavioural phase corresponds to the full clamping of all bolt rows and is named as "full contact condition", and it is characterised by $\frac{M/d_\gamma}{F_{pl}} < 1$.

The bending stiffness EI_1 is the bending stiffness of the channel web alone, EI_2 is the bending stiffness of the composite section (channel web + T-stub contribution), while EI_3 is the bending stiffness of the composite section (channel flange + upper/lower plate of nodal element). In this case, section AC is characterised by EI_2, section CD is characterised by EI_1, while the remaining part by EI_3.

In the case of Model 2 (see Fig. 22), the tensile force in the outermost bolt exceeds the initial preload, and separation occurs beyond section AB. The T-stub contribution vanishes, and only the channel web contributes. This scenario is named as "partial contact condition", and it is characterised by $\frac{M/d_\gamma}{F_{pl}} > 1$. In this case, section AB is characterised by EI_2, section BD is characterised by EI_1, while the remaining part by EI_3.

Table 5
Elastic stiffness, rotation, and resistance of the dissipative connection.

t_w [mm]	h [mm]	EI_1 [kNmm^2]	EI_2 [kNmm^2]	EI_3 [kNmm^2]	Two rows of bolts			Three rows of bolts		
					$\varphi_{B,Model1}$ [rad]	$\varphi_{B,Model2}$ [rad]	M (Eq.10) [kNm]	$\varphi_{B,Model1}$ [rad]	$\varphi_{B,Model2}$ [rad]	M (Eq.10) [kNm]
6	180	5.29E + 05	2.84E + 06	2.61E + 07	6.69E−03	1.20E−02	1.155	-	-	-
9		1.79E + 06	1.00E + 07	2.98E + 07	4.43E−03	7.91E−03	2.599	-	-	-
12		4.23E + 06	2.27E + 07	3.39E + 07	3.53E−03	6.14E−03	4.620	-	-	-
15		8.27E + 06	4.56E + 07	3.83E + 07	2.87E−03	4.94E−03	7.219	3.20E−03	6.59E−03	9.625
18		1.43E + 07	7.66E + 07	4.31E + 07	2.53E−03	4.26E−03	10.395	2.83E−03	5.68E−03	13.860
21		2.27E + 07	1.24E + 08	4.82E + 07	2.22E−03	3.71E−03	14.149	2.48E−03	4.96E−03	18.865
24		3.39E + 07	1.82E + 08	5.38E + 07	2.03E−03	3.36E−03	18.480	2.27E−03	4.48E−03	24.640
27		4.82E + 07	2.54E + 08	5.98E + 07	1.88E−03	3.09E−03	23.388	2.11E−03	4.12E−03	31.185

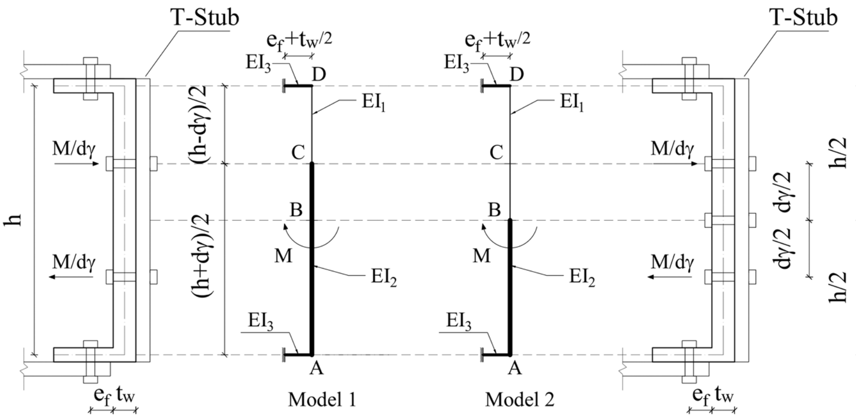

Fig. 22. Mechanical model to estimate the elastic rotation rigidity of the steel bolted channel.

For the sake of clarity, the analytical calculation of the bending stiffnesses of both full and partial contact conditions is reported in Appendix C. The calculated stiffnesses of the investigated connections are summarised in Table 5. In this regard, the geometrical parameters of the connections (which are needed to compute the rigidity) are given in Annex A. In particular, information about the T-stub element is reported in Figure A6, and that for the steel channel in Figure A7, while that corresponding to the upper and lower plates of the nodal element is given in Figure A8.

4.3. Evaluation of analytical predictions: comparison with FE results

Based on the mechanical models described in Sections 4.1 and 4.2, both the strength and stiffness are calculated, and the accuracy of those

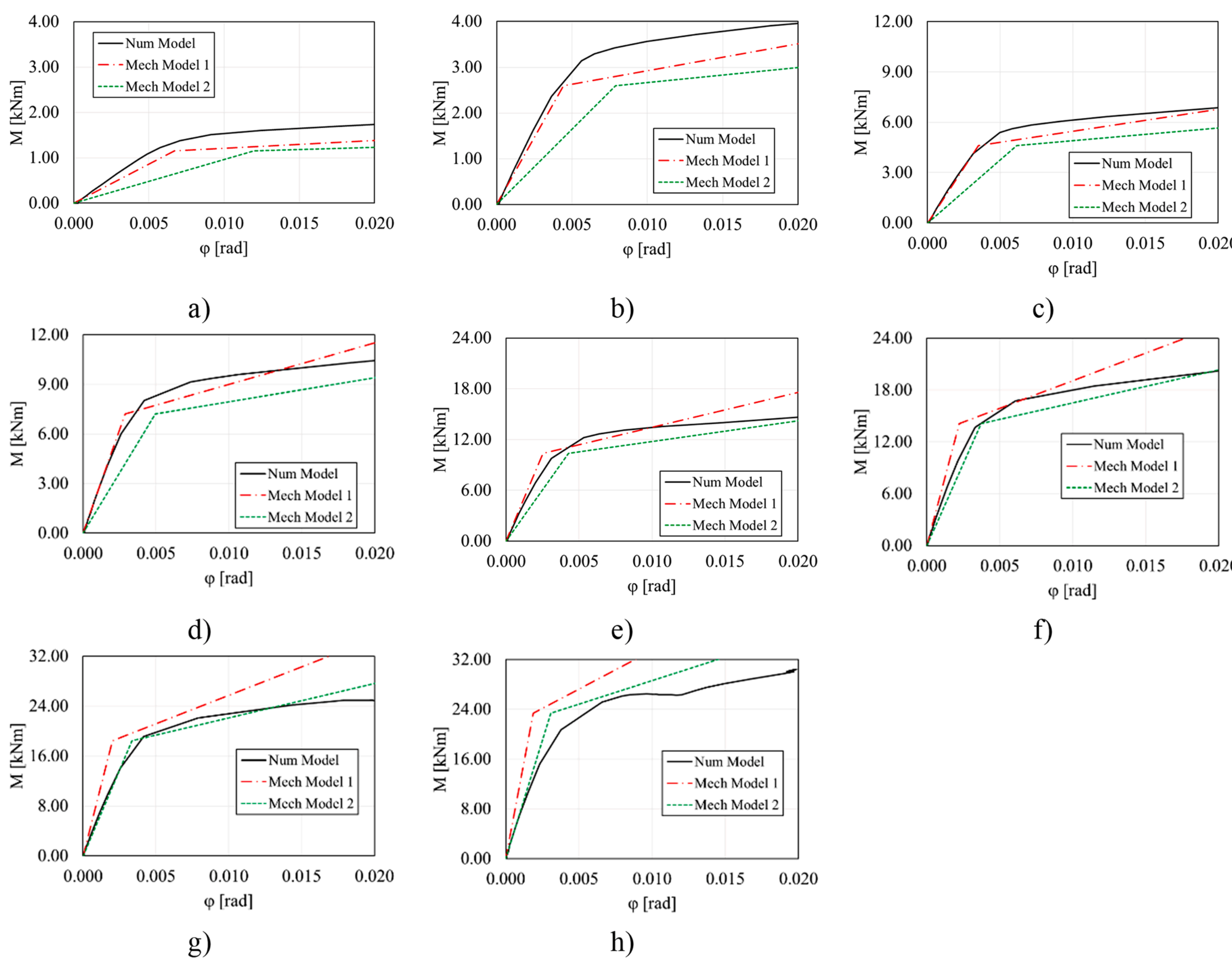

Fig. 23. Numerical and mechanical moment vs rotation curves obtained by varying the thickness of the web of the steel channel (t_w) for the case of two rows of two bolts: a) 6 mm; b) 9 mm; c) 12 mm; d) 15 mm; e) 18 mm; f) 21 mm; g) 24 mm; h) 27 mm.

predictions is shown in this section. The predicted values of the elastic rotational rigidity (evaluated at point B, see Fig. 22) and the plastic moment for the bolted channel connection are reported in Table 5. The proposed mechanical models allow the evaluation of the elastic response of the steel channel up to yielding. The post-yielding phase was schematized by considering a bi-linear response curve where the post-yielding stiffness (K_p) is assumed equal to $K_{el}/10$, following the ECCS−45 procedure for steel components [31].

Fig. 23 (two rows of two bolts) and 24 (three rows of two bolts) show the comparison between the analytical and numerical models in terms of moment M versus rotation φ curves, considering only the contribution of the steel channel and neglecting the GFRP beam. Moments are evaluated as described in Section 3.2, while the chord rotation φ of the steel channel is obtained by dividing the horizontal displacement at the upper row of bolts (point C) by the distance between this point and the bottom of the channel (point A).

The maximum rotation shown in the graphs is limited to 0.02 rad, due to the steel channel with a thickness of 27 mm (Fig. 23h), which, at this rotation, reaches a moment close to the theoretical ultimate moment of the GFRP beam (Section 3.3).

For the case of three bolt rows (see Fig. 24), the force on a single bolt is computed by dividing the resistance M from Table 5 by the bolt pitch (90 mm, see Appendix A – Figure A7b) and the number of bolts per row (two).

Tables 6 and 7 report the percentage differences between analytical and FE results obtained for the cases of two rows of bolts and three rows of bolts, respectively.

Figs. 23 and 24 and Tables 6 and 7 allow a consistent assessment of the analytical predictions against the FE results.

For the configuration with two bolt rows (Fig. 23), Model 1 provides an accurate prediction of both elastic stiffness and plastic resistance for web thicknesses up to 18 mm, with moment discrepancies generally below 8%. However, for larger thicknesses (21–27 mm), the numerical curves progressively deviate from Model 1 and are better reproduced by Model 2, with moment errors reduced below 6% and improved agreement in terms of elastic rotation.

The transition between Model 1 and Model 2 is clearly visible in Fig. 23e (t_w = 18 mm), where the FE curve lies between the two analytical predictions, indicating the onset of partial separation between the T-stub and the channel web.

A similar behaviour is observed for the configuration with three rows of two bolts (Fig. 24). In this case, Model 1 remains adequate up to t_w =24 mm, while for t_w =27 mm the numerical response is more consistent with Model 2, as confirmed by the reduction of the moment error reported in Table 7.

The transition between the two models is physically governed by the bolt preload condition. For relatively small web thicknesses, the tensile force per bolt remains below the preload force, ensuring full contact

Table 6
Percentage differences between analytical and FE results for two rows of bolts.

t_w [mm]	Model	Two rows of bolts	
		ΔM_{el} [%]	$\Delta\varphi_B$ [%]
6	1	8%	10%
9	1	8%	2%
12	1	8%	1%
15	1	2%	18%
18	1	6%	16%
18	2	6%	30%
21	2	6%	6%
24	2	6%	7%
27	2	4%	4%

Table 7
Percentage differences between analytical and FE results for three rows of bolts.

t_w [mm]	Model	Three rows of bolts	
		ΔM_{el} [%]	$\Delta\varphi_B$ [%]
15	1	18%	6%
18	1	13%	6%
21	1	10%	20%
24	1	5%	33%
24	2	5%	24%
27	2	7%	17%

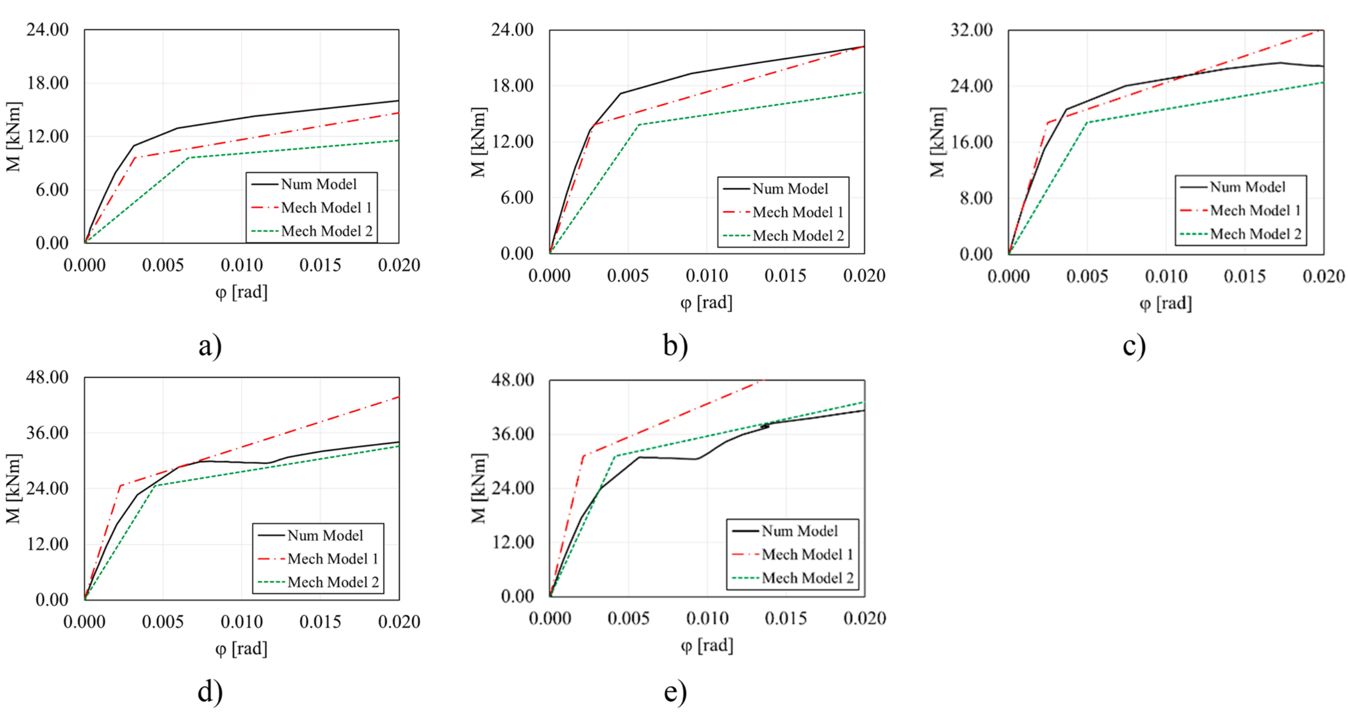

Fig. 24. Numerical and mechanical moment vs rotation curves obtained by varying the thickness of the web of the steel channel (t_w) for the case of three rows of two bolts: a) 15 mm; b) 18 mm; c) 21 mm; d) 24 mm; e) 27 mm.

between the T-stub and the channel web and activating the composite bending stiffness (Model 1). As the web thickness increases, the bending resistance of the channel increases accordingly, leading to higher tensile forces in the bolts that eventually exceed the preload force. This causes partial separation and loss of composite action, so that only the channel web contributes to bending stiffness (Model 2).

Overall, the comparison confirms that:

(i) the analytical strength prediction based on the plastic mechanism (Eq. 10) is satisfactorily accurate;
(ii) the stiffness prediction is sensitive to the contact condition due to the exceedance of clamping force in the outermost bolt row;
(iii) the mechanical interpretation based on bolt preload consistently explains the observed transition between Model 1 and Model 2.

4.4. Semi-empirical analytical model

An alternative approach for the evaluation of both the elastic and post-elastic behaviour of the structural fuse is the use of the semi-empirical two-stage Ramberg-Osgood analytical model. In the present study, it is employed as a phenomenological representation of the moment–rotation response previously obtained from finite element simulations. Its sole purpose is to supply a smooth analytical representation of the numerically obtained response, enabling straightforward implementation of the connection behaviour into common lumped non-linear springs that are typically used in global nonlinear structural analyses without the need for detailed finite element modelling.

Within the application of this method, it is possible to approximate the previously evaluated numerical results with a two-stage response curve (Fig. 25a and b), which is a function of several parameters, according to the expression given in Eq. 12.

$$\varphi = \begin{cases} \dfrac{\mu}{E} + 0.002\left(\dfrac{\mu}{\mu_y}\right)^n & \text{for } \mu \le \mu_y \\ \&\varphi_y + \dfrac{\mu - \mu_y}{E_p} + \left(\varphi_u - \varphi_y - \dfrac{\mu_u - \mu_y}{E_p}\right)\left(\dfrac{\mu - \mu_y}{\mu_u - \mu_y}\right)^m & \text{for } \mu_y < \mu \le \mu_u \end{cases} \tag{12}$$

The meaning of the symbols of Eq. (12) is clarified in Fig. 25c where μ_y is the normalized moment obtained by dividing the applied moment M over the maximum value M_u (which is assumed as the moment corresponding to an ultimate rotation of 0.02 rad in Figs. 23–24), φ_y is the corresponding rotation, μ_u is the ultimate normalized moment (equal to 1), φ_u is the corresponding ultimate rotation, E is the elastic stiffness while E_p is the post-elastic stiffness. Finally, the parameters $n = 12$ and $m = 3.64$ were calibrated to minimise the least-squares error with respect to the FE moment–rotation curves for the investigated geometries.

Fig. 25a–b show the comparison between FE results and the calibrated Ramberg–Osgood curves. The agreement confirms that the adopted formulation provides an accurate mathematical representation of the numerically determined behaviour within the considered rotation range.

5. Conclusions

In this study, the mechanical behaviour of recently patented hybrid FRP-to-steel joints was investigated. Finite element simulations, validated against experimental data, enabled a comprehensive

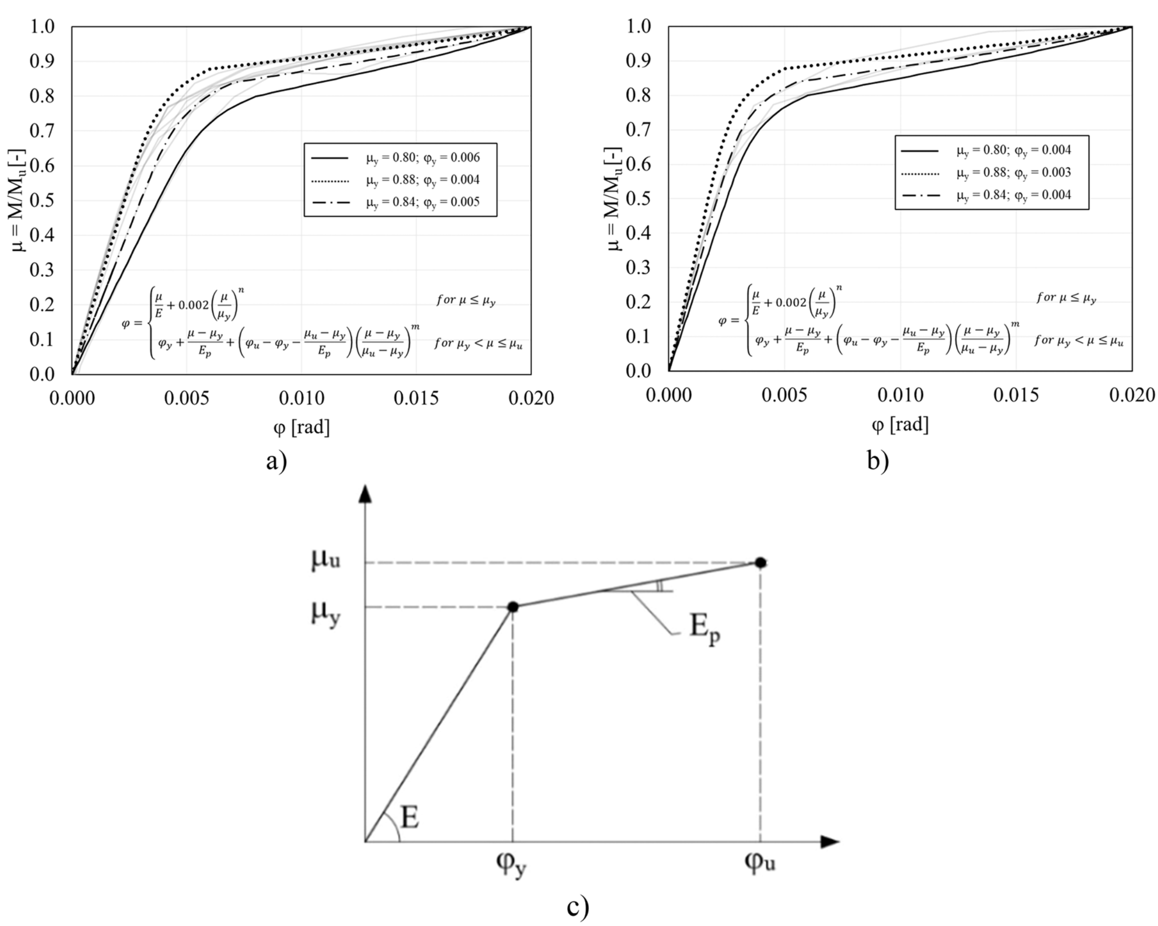

Fig. 25. Ramberg-Osgood model: a) Results for two rows of two bolts; b) Results for three rows of two bolts; c) Idealised bilinear response curve.

understanding of the joint's flexural response under varying geometric configurations. Based on the performed analyses, the following remarks can be drawn:

– The parametric FE analyses confirmed that the examined hybrid joints can guarantee large ductility and satisfactory resistance and rigidity.
– Increasing the thickness of the steel channel allows reaching flexural resistance close to the capacity of the connected pultrude profiles, but preserving their integrity, with the damage localised in the steel channel only.
– Analytical mechanical models have been developed to estimate the resistance and rigidity of the joints. The comparison with numerical response curves shows satisfactory accuracy.
– Semi-empirical Ramberg-Osgood-like analytical response curves have also been provided. These curves accurately match the expected response of the joints.
– Further experimental and numerical studies are needed to investigate the behaviour of the joints within the overall structural system, as well as against cyclic loading.

CRediT authorship contribution statement

Francesco Ascione: Conceptualization, Formal analysis, Methodology, Supervision, Validation, Writing – original draft, Writing – review & editing. **Mario D'Aniello:** Conceptualization, Formal analysis, Methodology, Supervision, Validation, Writing – original draft, Writing – review & editing. **Alessandro Leonardi:** Data curation, Formal analysis, Investigation, Software, Validation, Writing – original draft, Writing – review & editing.

Declaration of Competing Interest

The authors declare that they have no known competing financial interests or personal relationships that could have appeared to influence the work reported in this paper.

Appendix A

The dimensions of all elements constituting the connection are summarised in Figures A1-A8. In detail, Figures A1-A5 refer to the connection tested in the laboratory, while Figures A6-A8 refer to the connection upgraded to take into account the steel fuse thickness increase.

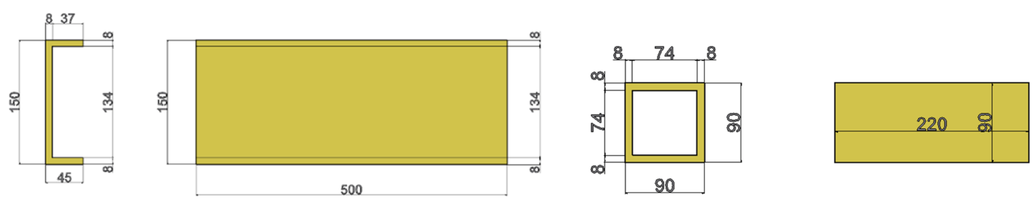

Fig. A1. Geometry of the GFRPs elements: channel profile for the beam and square hollow profile for the column.

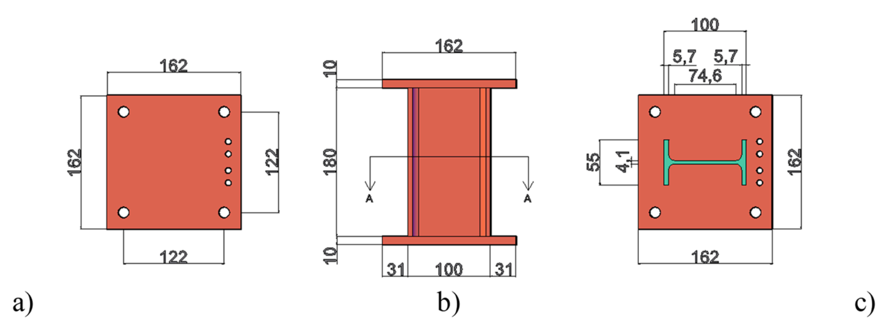

Fig. A2. Nodal element: a) end-plate (both topping and seating), b) I-profile, c) transverse section (A-A).

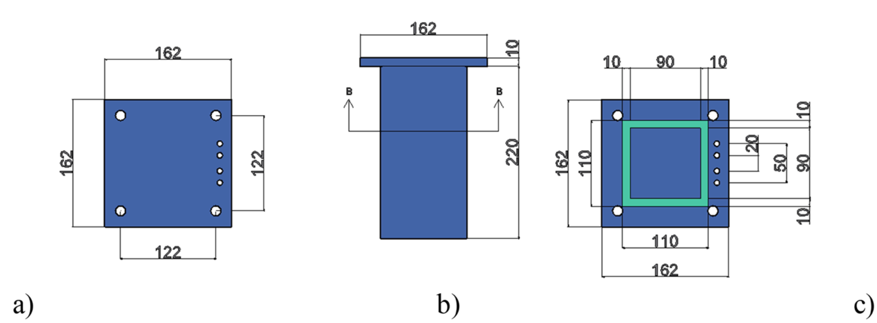

Fig. A3. Steel socket for column bonded connection: a) upper plate, b) socket, c) transverse section (B-B).

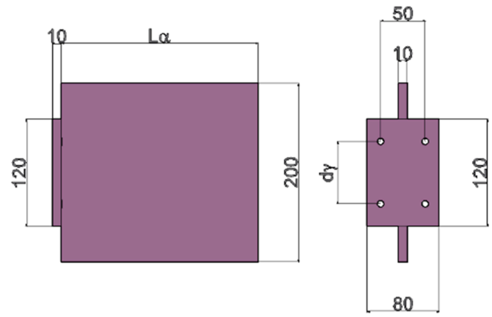

Fig. A4. Steel T-Stub to connect the GFRP beam to the steel channel (Lα and dγ variable). Lα=150– 220 while dγ=60 and 80 mm.

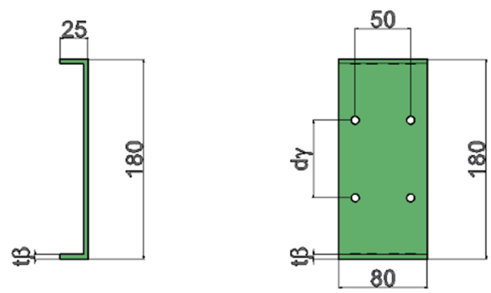

Fig. A5. Steel channel (tβ and dγ variable). tβ=2, 3, 4,5, 8 mm□.

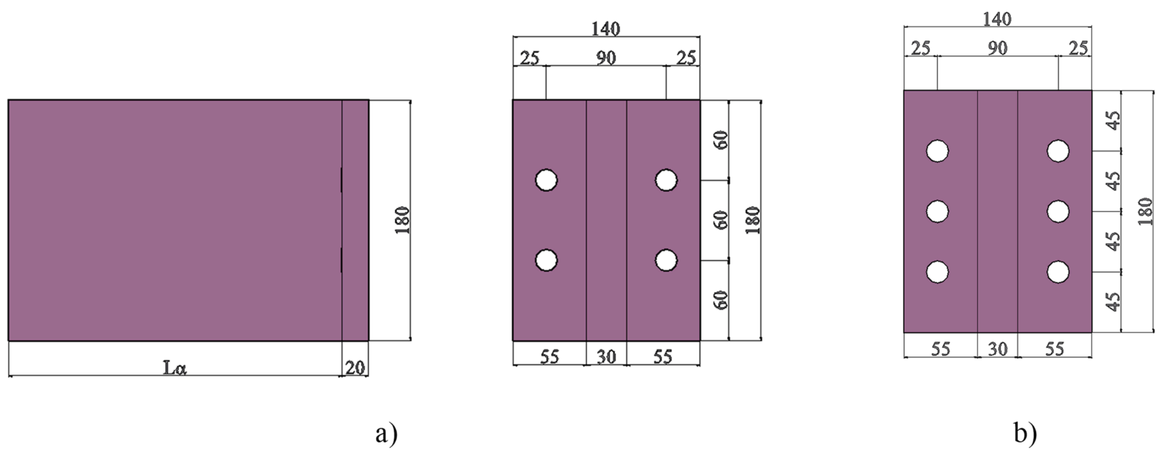

Fig. A6. Steel T-Stub upgraded to connect the GFRP beam to the steel channel (Section 3.3): a) two rows of two bolts; b) three rows of two bolts.

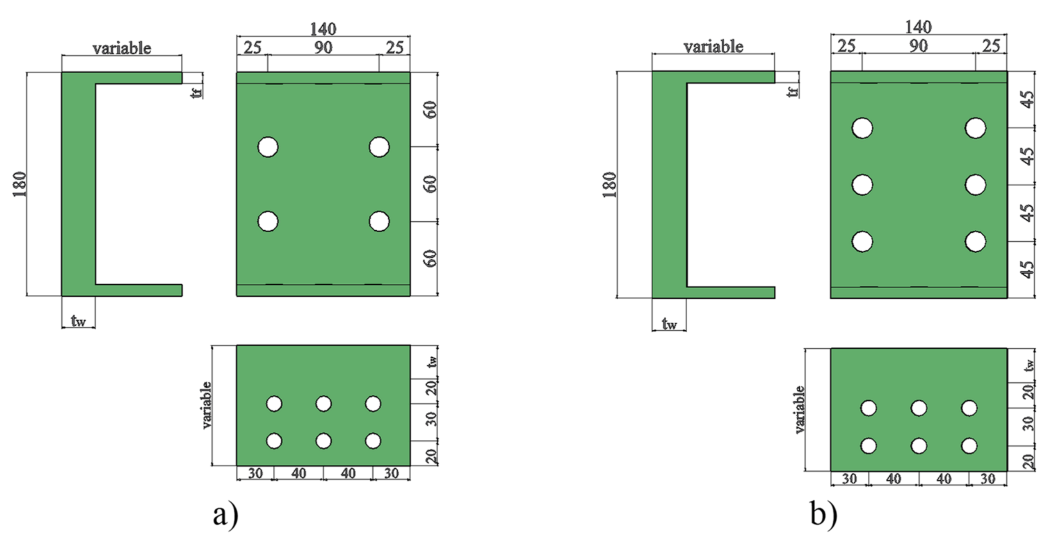

Fig. A7. Steel channel upgraded (Section 3.3): a) two rows of two bolts; b) three rows of two bolts.

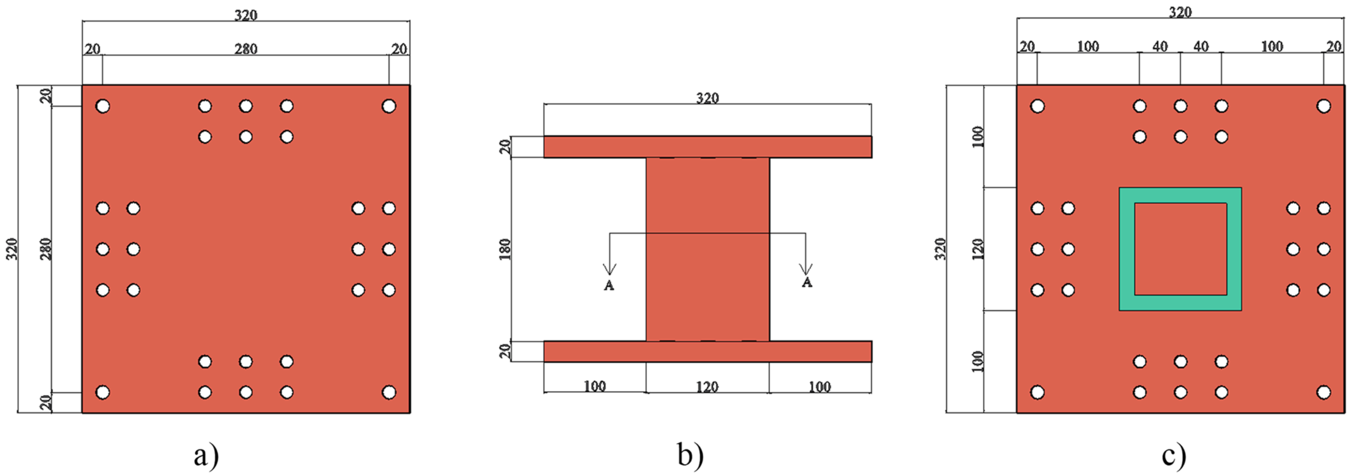

Fig. A8. Nodal element: a) end-plate (both topping and seating), b) Box-profile, c) transverse section (A-A).

.

Appendix B

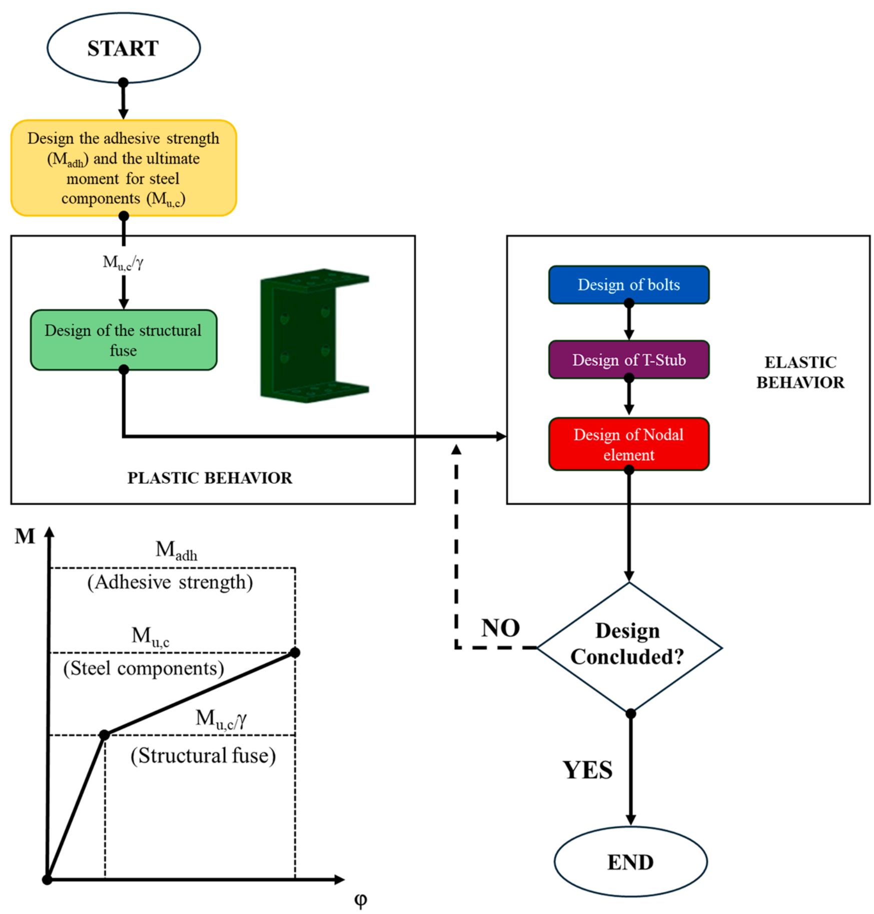

Fig. B1. Design process of steel components of the connection.

.

The design process of all the steel components is depicted in Figure B1. Once the adhesive strength in terms of failure moment (M_{adh}) is known, the ultimate moment for the steel components ($M_{u,c}$) is evaluated by dividing M_{adh} by a partial safety factor necessary to prevent the brittle failure of the connection. Then, the ultimate moment for the structural fuse, which must be the weakest element of the connection, is evaluated as $M_{u,c}/\gamma$, being γ a factor accounting for all sources of overstrength, set equal to 1.6 (Fig. 11a–b). Instead, all other steel elements will be designed in function of $M_{u,c}$.

According to the design process, the steel channel is firstly designed by adopting Eq. 5 presented in Section 4. Secondly, the resistance of the bolts connecting the web of the steel channel to the T-stub profile is verified according to Eurocode (2005) Part 1.8 [29], namely as follows:

$$\frac{F_{v,Ed}}{F_{v,Rd}}+\frac{F_{t,Ed}}{1,4\quad F_{t,Rd}}\leq 1 \tag{B.1}$$

$$\frac{F_{t,Ed}}{F_{t,Rd}}\leq 1 \tag{B.2}$$

In Eqn. (B.1) the terms assuming the following meaning: $F_{v,\ Ed}$ is the vertical force acting on the bolts evaluated by dividing moment M_{adh} by the lever arm of Fig. 2b (475 mm); $F_{t,\ Ed}$ is the tensile force acting on the bolts; $F_{v,\ Rd}$ and $F_{t,\ Rd}$ are the shear and tension resistance of the bolts, respectively. The latter are evaluated according to the following formula:

$$F_{v,Rd}=\frac{\alpha_v\, f_{ub}\, A_s}{\gamma_{M2}} \tag{B.3}$$

$$F_{t,Rd}=\frac{k\, f_{ub}\, A_s}{\gamma_{M2}} \tag{B.4}$$

The term A_s is the tensile stress area of the bolts, f_{ub} is the ultimate tensile strength of the bolts, γ_{M2} is the material partial factor, k is equal to 0,9, and α_v is equal to 0,5 for classes of bolts 4.8, 5.8, 6.8, and 10.9. For the sake of clarity, the case relative to the thickness of the web of the steel channel equal to 24 mm is reported in Table B1.

Table B1
Design of bolts on the web of the steel channel.

$A_{s\ (M16)}$	$f_{ub\ (CL10.9)}$	n_b	$F_{V,Rd}$	$F_{t,Rd}$	$F_{V,Ed}$	$F_{t,Ed}$	Eqn. B.1	Eqn. B.2
[mm^2]	[MPa]	[-]	[kN]	[kN]	[kN]	[kN]	[-]	[-]
157	1000	4	62.80	113.04	15.93	100.91	**0.89**	**0.89**

For what concerns the positioning of holes, they were evaluated according to the minimum and maximum spacing, end and edge distances defined by the Eurocode (2005) Part 1.8 [29]:

$$1,2\quad d_0\leq e_1\leq 4t+40\quad mm \tag{B.5}$$

$$1,2\quad d_0\leq e_2\leq 4t+40\quad mm \tag{B.6}$$

$$2,2\quad d_0\leq p_1\leq \min\{14t;.\quad 200mm\} \tag{B.7}$$

$$2,4\quad d_0\leq p_2\leq \min\{14t;.\quad 200mm\} \tag{B.8}$$

Where d_0 is the diameter of the hole, and t is the thickness of the thinner outer connected part. In Table B2 is reported the case relative to the thickness of the steel channel equal to 24 mm:

Table B2
Design of the position of holes on the web of the steel channel.

e_1	e_2	p_1	p_2
[mm]	[mm]	[mm]	[mm]
60	25	60	90

Instead, for the plates connected by the bolts, bearing and tension resistance was evaluated, according to Eurocode (2005) Part 1.8 [29]:

$$F_{b,Rd}=\frac{k_l\,\alpha_b\, f_u\, d\, t}{\gamma_{M2}} \tag{B.9}$$

$$F_{t,Rd}=\frac{0,9\quad A_{net}\, f_u}{\gamma_{M2}} \tag{B.10}$$

In Eqn. B.9 f_u is the tensile strength of the plate, d is the diameter of the bolt, t is the thickness of the thinner outer connected part and α_b and k_l are evaluated according to the following formula:

$$\alpha_b=\min\left\{\frac{f_u}{f_{ub}};.1\right\} \tag{B.11}$$

$$k_l=\min\left\{2,8\frac{e_2}{d_0}-1,7;.1,4\frac{p_2}{d_0}-1,7;.2,5\right\} \tag{B.12}$$

Instead, in Eq. B.10 A_{net} is obtained by removing the hole area from the cross-section of the plate.
Finally, the plates were designed according to Eqn. B.13 and B.14:

$$\frac{F_{v,Ed}}{F_{b,Rd}} \leq 1 \tag{B.13}$$

$$\frac{F_{v,Ed}}{F_{t,Rd}} \leq 1 \tag{B.14}$$

Where $F_{v,Ed}$ is the same as evaluated before.

Table B3 reports the case relative to the thickness of the steel channel equal to 24 mm:

Table B3
Evaluation of bearing and tension resistance of the plates connected.

k_l	α_b	$F_{b,Rd}$	A_n	$F_{t,Rd}$	$F_{V,Ed}$	Eqn. B.13	Eqn. B.14
[-]	[-]	[kN]	[mm^2]	[kN]	[kN]	[-]	[-]
2.4	1.0	204.24	2544	666.29	15.93	**0.07**	**0.05**

Then, the same process was repeated for the bolts that connect the flange of the steel channel to the upper and lower plates of the steel core. The bolts were designed according to Eurocode (2005) Part 1.8 [30]:

$$\frac{F_{v,Ed}}{F_{v,Rd}} \leq 1 \tag{B.15}$$

In this case, the bolts were subjected only to a shear force, obtained by dividing the moment by the height of the nodal element. For the sake of clarity, the case relative to the thickness of the web of the steel channel equal to 24 mm is reported in Tables B4-B6.

Table B4
Design of bolts on the flange of the steel channel.

$A_{s\ (M12)}$	$f_{tb\ (CL10.9)}$	n_b	$F_{V,Rd}$	$F_{V,Ed}$	Eqn. B.15
[mm^2]	[MPa]	[-]	[kN]	[kN]	[-]
84	1000	6	33.50	28.03	**0.84**

Table B5
Design of the holes position on the flange of the steel channel.

e_1	e_2	p_1	p_2
[mm]	[mm]	[mm]	[mm]
20	30	30	40

In addition to the tensile strength check evaluated according to Eqn. B.14, for the flange of the steel channel, it is also necessary to verify the shear strength, in order to avoid brittle failures and guarantee.

the sufficient ductile behaviour required by the plastic hinge, located in this section. According to Eurocode 3 [32], the design shear resistance is given by:

$$V_{c,Rd} = \frac{A_v \left(f_y \;\Big/\; \sqrt{3}\right)}{\gamma_{M0}} \tag{B.16}$$

In Eqn. B.16 A_v is the shear area, while f_y is the tensile yield strength of the steel. The check was performed according to Eqn. B.17:

$$\frac{V_{Ed}}{V_{c,Rd}} \leq 1 \tag{B.17}$$

Where V_{Ed} is the vertical force evaluated by dividing the moment by the lever arm of Fig. 2b (475 mm). In Table B6 are reported both the Eqn. B.14 and B.17.

Table B6
Evaluation of tension and shear resistance of the flange of the structural fuse.

A_n	$F_{t,Rd}$	A_v	$V_{c,Rd}$	$F_{V,Ed}$	V_{Ed}	Eqn. B.14	Eqn. B.17
[mm^2]	[kN]	[mm^2]	[kN]	[kN]	[kN]	[-]	[-]
832	217.90	1120	169.36	28.03	63.73	**0.39**	**0.38**

After designing bolts, it is necessary to design the steel T-Stub by applying the Equivalent T-Stub in tension model, considering the bolt row as an individual element. In particular, according to Eurocode (2005) Part 1.8 [29], the effective lengths of this element, for an end bolt row, are evaluated as follows:

$$l_{eff,1} = l_{eff,nc} \text{but} l_{eff,1} \leq l_{eff,cp} \tag{B.18}$$

$$l_{eff,2} = l_{eff,nc} \tag{B.19}$$

Where $l_{eff,1}$ and $l_{eff,2}$ are, respectively, the effective length of the T-Stub considering the failure in Mode 1 (complete yielding of the flange) or in Mode 2 (bolt failure with yielding of the flange), function of $l_{eff,cp}$ and $l_{eff,nc}$ that are evaluated as follows

$$l_{eff,cp} = \min \quad \{2\pi\, m; \pi\, m + 2e_1\} \tag{B.20}$$

$$l_{eff,nc} = \min \quad \{4m + 1,25e; 2m + 0,625 \quad e + e_1\} \tag{B.21}$$

In details, the terms $l_{eff,cp}$ and $l_{eff,nc}$ are function of the two possible model patterns (circular or non-circular), e_1 is the distance from the center of the fasteners in the end row to the adjacent free end of the flange measured in the direction of the axis of the profile, while the geometrical parameters "m" and "e", which is equal to "e_{min}", are referred to the cross section of the T-Stub.

Then it is possible to evaluate the three values of the resistance of the T-Stub ($F_{T,1,Rd}$, $F_{T,2,Rd}$, $F_{T,3,Rd}$) for the two modes explained before and for the third one, which corresponds to the bolt failure:

$$F_{T,1,Rd} = \min \quad \left\{\frac{4 \quad M_{pl,1,Rd}}{m}; \frac{(8n - 2e_w) \quad M_{pl,1,Rd}}{2m\, n - e_w(m+n)}\right\} \tag{B.22}$$

$$F_{T,2,Rd} = \frac{2 \quad M_{pl,2,Rd} + n\sum F_{t,Rd}}{m+n} \tag{B.23}$$

$$F_{T,3,Rd} = \sum F_{t,Rd} \tag{B.24}$$

Where $\sum F_{t,Rd}$ is the design tension resistance for all the bolts in the T-stub, while the other parameters are defined as follows:

$$e_w = \frac{d_w}{4} \tag{B.25}$$

$$n = e_{\min} \text{but} n \leq 1,25 \quad m \tag{B.26}$$

$$M_{pl,1,Rd} = 0,25 \quad l_{eff,1} \quad \frac{t_f^2 f_y}{4} \tag{B.27}$$

$$M_{pl,1,Rd} = 0,25\, l_{eff,2} \quad \frac{t_f^2 f_y}{4} \tag{B.28}$$

In which d_w is the diameter of the washer, e_{min} was introduced before, t_f is the thickness of the T-Stub and f_y is the tensile yield strength of the steel. Finally, it should be verified that:

$$\frac{F_{t,Ed}}{\min\{F_{T,1,Rd}; F_{T,2,Rd}; F_{T,3,Rd}\}} \leq 1 \tag{B.29}$$

According to Table B1, in Table B7 the numerical values of the design of the steel T-Stub are reported for the case relative to the thickness of the web of the steel channel equal to 24 mm.

Table B7
Design of T-Stub.

f_y	t_f	d_w	e_w	m	e	e_1	n
[MPa]	[mm]	[mm]	[mm]	[mm]	[mm]	[mm]	[mm]
275	20	30	7.5	30	25	60	25

$L_{eff,cp}$	$L_{eff,nc}$	$L_{eff,1}$	$L_{eff,2}$	$M_{pl,1,Rd}$	$M_{pl,2,Rd}$
[mm]	[mm]	[mm]	[mm]	[kNmm]	[kNmm]
188	136	136	136	3729.68	3729.68

$F_{T,1,Rd}$	$F_{T,2,Rd}$	$F_{T,3,Rd}$	$F_{T,Ed}$	Eqn. B.29
[kN]	[kN]	[kN]	[kN]	[-]
497.29	238.39	226.08	201.81	**0.89**

Finally, the steel core was designed taking into account bending and shear effects, according to the following formulas of the Eurocode (2005) Part 1.1 [32]:

$$\frac{M_{Ed}}{M_{c,Rd}} \leq 1 \tag{B.30}$$

$$\frac{V_{Ed}}{V_{c,Rd}} \leq 1 \tag{B.31}$$

In which M_{Ed} is the design moment, V_{Ed} is the shear design force acting on the nodal element, evaluated by dividing design moment by the height of the nodal element, while $M_{c,Rd}$ and $V_{c,Rd}$ are respectively the design resistance for bending about one principal axis of a cross-section and the design shear resistance. The latter are evaluated according to the following formulas:

$$M_{C,Rd} = \frac{W_{el} f_y}{\gamma_{M0}} \tag{B.32}$$

$$V_{C,Rd} = \frac{A_v f_y}{\sqrt{3}\gamma_{M0}} \tag{B.33}$$

Where W_{el} is the elastic section modulus of the profile, and A_v is the shear area. The profile selected is a hollow profile 120x120x15.

According to Table B1 and Table B7, in Table B8 the numerical values of the design of the nodal element are reported for the case of the thickness of the web of the steel channel equal to 24 mm.

Table B8
Design of nodal element.

$V_{c,Rd}$	$M_{c,Rd}$	V_{Ed}	M_{Ed}	Eqn. B.32	Eqn. B.33
[kN]	[kNm]	[kN]	[kNm]	[-]	[-]
408.27	51.6	168.2	30.0	**0.59**	**0.41**

Appendix C

With reference to the static scheme of Fig. 22, the elastic rotation at point B was evaluated through the principle of virtual power. Its analytical expression is reported hereinafter.

$$\varphi_B = \left[\frac{M}{(EI)_3}a + \frac{M}{(EI)_1}b\right] + \overline{X}_1\left[-\frac{1}{2(EI)_3}a^2 - \frac{1}{(EI)_1}ab\right] + \overline{X}_2\left[\frac{1}{2(EI)_2}b^2 - \frac{1}{(EI)_2}ah - \frac{1}{(EI)_2}bh\right] + \overline{X}_3\left[-\frac{1}{(EI)_3}a - \frac{1}{(EI)_3}b\right] \tag{C.1}$$

In Eqn. (C1), the symbols assume the following meaning with reference to Fig. 22: M is the applied moment at point B, *h* is the web channel length, while terms $(EI)_i$ are the bending stiffness. Furthermore, for the sake of brevity, all other symbols are a collection of different terms function of geometry as well as shear (GA), bending (EI) and axial (EA) stiffness of each part of the structural scheme of Fig. 22.

$$a = \left(e_f + \frac{t_w}{2}\right), \quad b = \left(\frac{h - d_\gamma}{2}\right), \quad c = \left(\frac{h + d_\gamma}{2}\right) \tag{C.2a-c}$$

$$\overline{X}_3 = \frac{\delta_1 \quad \alpha_2 \quad \varphi\,\mu}{\alpha_1\;\epsilon\,A} - \frac{\delta_2 \quad \varphi}{A} + \frac{\delta_1 \quad \alpha_3}{\alpha_1\;\epsilon\,A} - \frac{\delta_3}{\epsilon\,A} \tag{C.3}$$

$$\overline{X}_2 = \overline{X}_3\left(\frac{\gamma_1 \quad \alpha_2 \quad \varphi}{\alpha_1} - \delta_2 \quad \varphi\right) + \frac{\delta_1 \quad \alpha_2 \quad \varphi}{\alpha_1} - \delta_2 \quad \varphi \tag{C.4}$$

$$\overline{X}_1 = -\overline{X}_2\frac{\beta_1}{\alpha_1} - \overline{X}_3\frac{\gamma_1}{\alpha_1} - \frac{\delta_1}{\alpha_1} \tag{C.5}$$

$$A = 1 - \frac{\gamma_1 \quad \alpha_2 \quad \varphi\,\mu}{\alpha_1\;\varepsilon} + \frac{\delta_2 \quad \varphi\,\mu}{\varepsilon} \tag{C.6}$$

$$\varepsilon = \gamma_3 - \frac{\gamma_1 \quad \alpha_3}{\alpha_1}, \mu = \beta_3 + \frac{\beta_1 \quad \alpha_3}{\alpha_1}, \varphi = \left(\beta_2 - \frac{\beta_1 \quad \alpha_2}{\alpha_1}\right)^{-1} \tag{C.7a-c}$$

$$\alpha_1 = \frac{a^3}{3(EI)_3} + \frac{a}{(GA)_3} + \frac{a^2\,b}{(EI)_1} + \frac{b}{(EA)_1} - \frac{a\,b\,c}{(EI)_2} + \frac{a\,h\,c}{(EI)_2} + \frac{a\,c^2}{2(EI)_2} + \frac{a^3}{3(EI)_1} + \frac{a}{(GA)_1} \tag{C.8}$$

$$\beta_1 = \frac{a^2\,h}{2(EI)_3} + \frac{a\,b\,h}{(EI)_1} - \frac{b^2\,a}{2(EI)_1} - \frac{c\,b^2}{(EI)_2} - 2\frac{h\,b\,c}{(EI)_2} - \frac{3}{2}\frac{b\,c^2}{(EI)_2} + \frac{c\,h^2}{(EI)_2} + \frac{h\,c^2}{2(EI)_2} + \frac{c^3}{3(EI)_2} + \frac{c}{(EA)_2} \tag{C.9}$$

$$\gamma_1 = \frac{a^2}{2(EI)_3} - \frac{b\,c}{(EI)_2} + \frac{a^2}{2(EI)_1} \tag{C.10}$$

$$\delta_1 = -\frac{M\,a^2}{2(EI)_3} - \frac{M\,a\,b}{(EI)_1} \tag{C.11}$$

$$\alpha_2 = \frac{a^2\,h}{2(EI)_3} + \frac{a\,b\,h}{(EI)_1} - \frac{b^2\,a}{2(EI)_1} - \frac{a\,b\,c}{(EI)_2} + \frac{a\,h\,c}{(EI)_2} + \frac{a\,c^2}{2(EI)_2} \tag{C.12}$$

$$\beta_2 = \frac{h^2\,a}{(EI)_3} + \frac{a}{(EA)_3} + \frac{b\,h^2}{(EI)_1} - \frac{b^2\,h}{2(EI)_1} - \frac{b^3}{3(EI)_1} - \frac{b}{(GA)_1} - \frac{c\,b^2}{(EI)_2} - 2\frac{b\,c\,h}{(EI)_2} + \frac{c\,h^2}{(EI)_2} + \frac{h\,c^2}{(EI)_2} - \frac{c^3}{3(EI)_2} + \frac{c}{(GA)_2} + \frac{a}{(EA)_2} \tag{C.13}$$

$$\gamma_2 = \frac{a\,h}{(EI)_3} + \frac{b\,h}{(EI)_1} - \frac{b^2}{2(EI)_1} - \frac{b\,c}{(EI)_2} + \frac{c\,h}{(EI)_2} + \frac{c^2}{2(EI)_2} \tag{C.14}$$

$$\delta_2 = -\frac{M\,a\,h}{(EI)_3} - \frac{M\,h\,b}{(EI)_1} + \frac{M\,b^2}{2(EI)_1} \tag{C.15}$$

$$\alpha_3 = \frac{a^2}{(EI)_3} + \frac{a\,b}{(EI)_1} + \frac{a\,c}{(EI)_2} \tag{C.16}$$

$$\beta_3 = \frac{a\,h}{(EI)_3} + \frac{b\,h}{(EI)_1} - \frac{b^2}{2(EI)_1} + \frac{c\,h}{(EI)_2} + \frac{c^2}{2(EI)_2} \tag{C.17}$$

$$\gamma_3 = 2\frac{a}{(EI)_3} + \frac{b}{(EI)_1} + \frac{c}{(EI)_2} \tag{C.18}$$

$$\delta_3 = -\frac{M\,a}{(EI)_3} - \frac{M\,b}{(EI)_1} \tag{C.19}$$

From Eqn. (C1), it is possible to split the solution between model 1 and model 2 by imposing $d_\gamma \neq 0$ or $d_\gamma = 0$ (see Fig. 22), respectively. In the first case, the expressions of parameters b and c are those of Eqn. (C2b,c) while, in the second case, they both assume the value equal to $h/2$.

References

[1] CEN/TS 19101: 2022. Design of fibre-polymer composite structures.

[2] J. Qureshi, J.T. Mottram, Behaviour of pultruded beam-to-column joints using steel web cleats, Thin-Walled Struct. 73 (2013) 48–56, https://doi.org/10.1016/j.tws.2013.06.019.

[3] J. Qureshi, J.T. Mottram, Response of beam-to-column web cleated joints for FRP pultruded members, J. Compos Constr. (2014) 18, https://doi.org/10.1061/(ASCE)CC.1943-5614.0000392.

[4] J. Qureshi, J.T. Mottram, Moment-rotation response of nominally pinned beam-to-column joints for frames of pultruded fibre reinforced polymer, Constr. Build. Mater. 77 (2015) 396–403, https://doi.org/10.1016/j.conbuildmat.2014.12.057.

[5] J.L. Clarke, Structural Design Of Polymer Composites: EUROCOMP Design Code and Handbook, E & FN Spon, London, 1996.

[6] D. Martins, J.R. Correia, J. Gonilha, M. Arruda, N. Silvestre, Development of a novel beam-to-column connection system for pultruded GFRP tubular profiles, Compos Struct. 171 (2017) 263–276, https://doi.org/10.1016/j.compstruct.2017.03.049.

[7] S. Russo, On failure modes and design of multi-bolted FRP plate in structural joints, Compos Struct. 218 (2019) 27–38, https://doi.org/10.1016/j.compstruct.2019.03.048.

[8] F.J. Luo, Y. Huang, X. He, Y. Qi, Y. Bai, Development of latticed structures with bolted steel sleeve and plate connection and hollow section GFRP members, Thin-Walled Struct. 137 (2019) 106–116, https://doi.org/10.1016/j.tws.2018.12.036.

[9] D. Martins, J. Gonilha, J.R. Correia, N. Silvestre, Monotonic and cyclic behaviour of cuff beam-to-column connection system for tubular pultruded GFRP profiles, Eng. Struct. (2021) 247, https://doi.org/10.1016/j.engstruct.2021.113165.

[10] D. Martins, J. Gonilha, J.R. Correia, N. Silvestre, Monotonic and cyclic behaviour of a stainless steel cuff system for beam-to-column connections between pultruded I-section GFRP profiles, Eng. Struct. (2021) 249, https://doi.org/10.1016/j.engstruct.2021.113294.

[11] D. Martins, J. Gonilha, J.R. Correia, N. Silvestre, Exterior beam-to-column bolted connections between GFRP I-shaped pultruded profiles using stainless steel cleats. Part 1: Experimental study, Thin-Walled Struct. (2021) 163, https://doi.org/10.1016/j.tws.2021.107719.

[12] D. Martins, J. Gonilha, J.R. Correia, N. Silvestre, Exterior beam-to-column bolted connections between GFRP I-shaped pultruded profiles using stainless steel cleats, Part 2: Prediction of initial stiffness and strength, Thin-Walled Struct. (2021) 164, https://doi.org/10.1016/j.tws.2021.107762.

[13] G. Ferrara, O. Helson, L. Michel, E. Ferrier, Mechanical characterisation of GFRP frame and beam-to-column joints including steel plate fastened connections, Materials (2022) 15, https://doi.org/10.3390/ma15238282.

[14] S. Singamsethi, J. LaFave, K. Hjelmstad, Fabrication and testing of cuff connections for GFRP box sections, J. Compos. Constr. 9 (6) (2005) 536–544, https://doi.org/10.1061/(ASCE)1090-0268(2005)9:6(536).

[15] Carrion J.E., LaFave J., Hjelmstad K. Experimental behavior of monolithic composite cuff connections for fiber reinforced plastic box sections, 2005. https://doi.org/10.1016/j.compstruct.2004.01.015.

[16] F. Ascione, M. Lamberti, A.G. Razaqpur, S. Spadea, Strength and stiffness of adhesively bonded GFRP beam-column moment resisting connections, Compos Struct. 160 (2017) 1248–1257, https://doi.org/10.1016/j.compstruct.2016.11.021.

[17] A.G. Razaqpur, F. Ascione, M. Lamberti, S. Spadea, M. Malagic, GFRP hollow column to built-up beam adhesive connection: mechanical behaviour under quasi-static, cyclic and fatigue loading, Compos Struct. (2019) 224, https://doi.org/10.1016/j.compstruct.2019.111069.

[18] F. Ascione, L. Granata, G. Carozzi, Flexural and shear behaviour of adhesive connections for large scale GFRP frames: influence of the bonded area and hygrothermal aging, Compos Struct. (2022) 283, https://doi.org/10.1016/j.compstruct.2021.115122.

[19] Z. Zhang, C. Wu, X. Nie, Y. Bai, L. Zhu, Bonded sleeve connections for joining tubular GFRP beam to steel member: numerical investigation with experimental validation, Compos Struct. 157 (2016) 51–61, https://doi.org/10.1016/j.compstruct.2016.08.016.

[20] C. Wu, Z. Zhang, Y. Bai, Connections of tubular GFRP wall studs to steel beams for building. Construction, Comp. Part B 95 (2016) 64–75, https://doi.org/10.1016/j.compositesb.2016.03.081.

[21] Zhang Z.J., Bai Y., Xiao X. Bonded Sleeve Connections for Joining Tubular Glass Fiber–Reinforced Polymer Beams and Columns: Experimental and Numerical Studies, 2018. https://doi.org/10.1061/(ASCE)CC.1943–5614.0000853.

[22] C. Qiu, Y. Bai, L. Zhang, L. Jin, Bending performance of splice connections for assembly of tubular section FRP members: experimental and numerical study, J. Compos. Constr. 23 (5) (2019), https://doi.org/10.1061/(ASCE)CC.1943-5614.0000964.

[23] P. Feng, Y. Wu, Y. Ding, T.Q. Liu, Y. Tian, Quasi-plastic flexural behavior of adhesive-bolt hybrid connection for large scale pultruded GFRP frame, Eng. Struct. (2021) 238, https://doi.org/10.1016/j.engstruct.2021.112200.

[24] F. Ascione, M. D'Aniello, L. Feo, L. Granata, R. Landolfo, A novel ductile connection for FRP pultruded beam-to-column assemblies, Compos Struct. (2024) 337, https://doi.org/10.1016/j.compstruct.2024.118091.

[25] Top Glass Industries S.p.A; ⟨https://www.topglass.com/⟩.

[26] Araldite technical data sheet; 2020; ⟨https://www.huntsman.com⟩.

[27] F. Ascione, L. Granata, L. Guadagno, C. Naddeo, Hygrothermal durability of epoxy adhesives used in civil structural applications, Compos Struct. (2021) 265, https://doi.org/10.1016/j.compstruct.2021.113591.

[28] Abaqus 6.14–4. (2014). Dassault Systèmes Simulia Corp., Providence, RI.

[29] M. D'Aniello, D. Cassiano, R. Landolfo, Simplified criteria for finite element modelling of European preloadable bolts, Steel Compos Struct. 24 (6) (2017) 643–658, https://doi.org/10.12989/scs.2017.24.6.643.

[30] EN 1993–1-8: 2024. Eurocode 3 – Design of Steel Structures Part 1–8: joints.

[31] ECCS-45 - European convention for constructional steelwork, Recommended Testing Procedure for Assessing the Behaviour of Steel Elements Under Cyclic Loads, Brussels, 1986.

[32] EN 1993: 2005. Eurocode 3 Part 1–1: General rules and rules for buildings.